Journal of Geophysical Research: Atmospheres

RESEARCH ARTICLE
10.1029/2018JD028561

Dynamics and Predictability of the Rapid Intensification of Super Typhoon Usagi (2013)

Su Liu[1,2,3], Dandan Tao[3], Kun Zhao[1,2], Masashi Minamide[3], and Fuqing Zhang[3]

[1]Key Lab of Mesoscale Severe Weather/Ministry of Education of China, School of Atmospheric Sciences, Nanjing University, Nanjing, China, [2]State Key Laboratory of Severe Weather, Joint Center for Atmospheric Radar Research of CMA/NJU, Beijing, China, [3]Department of Meteorology and Atmospheric Science, Center for Advanced Data Assimilation and Predictability Techniques, The Pennsylvania State University, University Park, PA, USA

Key Points:
- The predictability of the rapid intensification of Super Typhoon Usagi (2013) was mainly determined by the initial conditions of the vortex
- Assimilating atmospheric motion vectors can improve tropical cyclone vortex intensity and further improve the rapid intensification forecast
- Uncertainties in tropical cyclone initial inner-core moisture can impact the intensification process

Correspondence to:
K. Zhao,
zhaokun@nju.edu.cn

Citation:
Liu, S., Tao, D., Zhao, K., Minamide, M., & Zhang, F. (2018). Dynamics and predictability of the rapid intensification of Super Typhoon Usagi (2013). *Journal of Geophysical Research: Atmospheres*, *123*. https://doi.org/10.1029/2018JD028561

Received 22 FEB 2018
Accepted 16 JUN 2018
Accepted article online 27 JUN 2018

Abstract This study explores the dynamics and predictability of the rapid intensification (RI) of Super Typhoon Usagi (2013) through a 60-member convection-permitting ensemble using the Weather Research and Forecasting (WRF) model and an ensemble Kalman filter (EnKF) data assimilation method. The surface maximum wind speed of Usagi, which was an intense category 4 western North Pacific tropical cyclone (TC), increased by 33 m s^{-1} over a 24-hr period. The RI process was captured by the WRF simulation initialized with the global analysis but with a unique forecast challenge of early prediction. We improved the intensity forecasts by assimilating satellite-derived atmospheric motion vectors into the WRF-EnKF, which primarily reduced the strength of both the primary and secondary circulations in the TC vortex. Nevertheless, our ensemble forecasts initialized with the EnKF analysis ensemble predicted a significant spread in the intensity with considerable differences in the RI onset timing among individual members. Our analyses show that variation in the RI timing is most sensitive to differences in the initial TC vortex intensity and inner-core moisture. Ensemble members with similar initial intensities but greater tropospheric moisture content exhibited earlier vortex axisymmetrization and consequently earlier RI. Further sensitivity experiments showed that variations in the inner-core moisture content have an immediate impact on the structure and strength of inner-core convection. These variations in inner-core convection gradually caused differences in intensity between the TC vortices. In this study, we highlight the importance of accurate estimates of the inner-core moisture content in the modeling and forecasting of TC intensity.

1. Introduction

Over the last decade, much effort from the research and operation communities has been directed toward improving tropical cyclone (TC) intensity forecasting. However, it is still challenging to predict significant changes in the intensity of a TC, such as rapid intensification (RI) or rapid decay (DeMaria et al., 2014).

In this study, we focused on Super Typhoon Usagi (2013), which was one of the most intense western North Pacific TCs (equivalent to a category 4 hurricane on the Saffir-Simpson hurricane wind scale) in the year 2013. The storm, which was monitored by the Japan Meteorological Agency, was a tropical depression located about 1,300 km east of the Philippines at 0000 UTC 16 September. After 0000 UTC 18 Sep, Usagi moved west along the southern periphery of the western North Pacific Subtropical High (WNPSH), with a speed of 10–20 mph. The storm developed over extremely warm water (>30°C, Figure 1b) within an environment with weak vertical wind shear (4 m s^{-1}). At 0600 UTC 18 September, Usagi began a 30-hr period of explosive intensification and formed a 28-km diameter round eye that was clearly visible in satellite images (Figure 1c). The maximum wind speed (V_{max}) increased by 33 m s^{-1} over the 24-hr period, which was more than twice of the common threshold for defining RI, which is 15 m s^{-1} (30 knot) d^{-1} (NASA, 2013). At 1800 UTC 19 September, Usagi reached its peak intensity, with a 10-min maximum sustained wind velocity of 57 m s^{-1} and minimum sea level pressure (minSLP) of 910 hPa. An eyewall replacement cycle began at 0800 UTC on 20 September. The storm started to weaken on the same day, as it interacted with the islands of Taiwan and Luzon, but then reintensified and evolved into a triple-eyewall structure at 2000 UTC 21 September (Zhao et al., 2016). Previous studies have shown that convection-permitting regional forecasts often miss TC intensification processes if they use the results from global analysis directly as initial conditions (ICs; e.g., Liu & Li, 2010; Weng & Zhang, 2012). However, Usagi presents a unique forecasting challenge because the convection-permitting forecast predicted the RI process far too early (the control run, CNTL, in Figure 2). This is one of the primary motivations of this study.

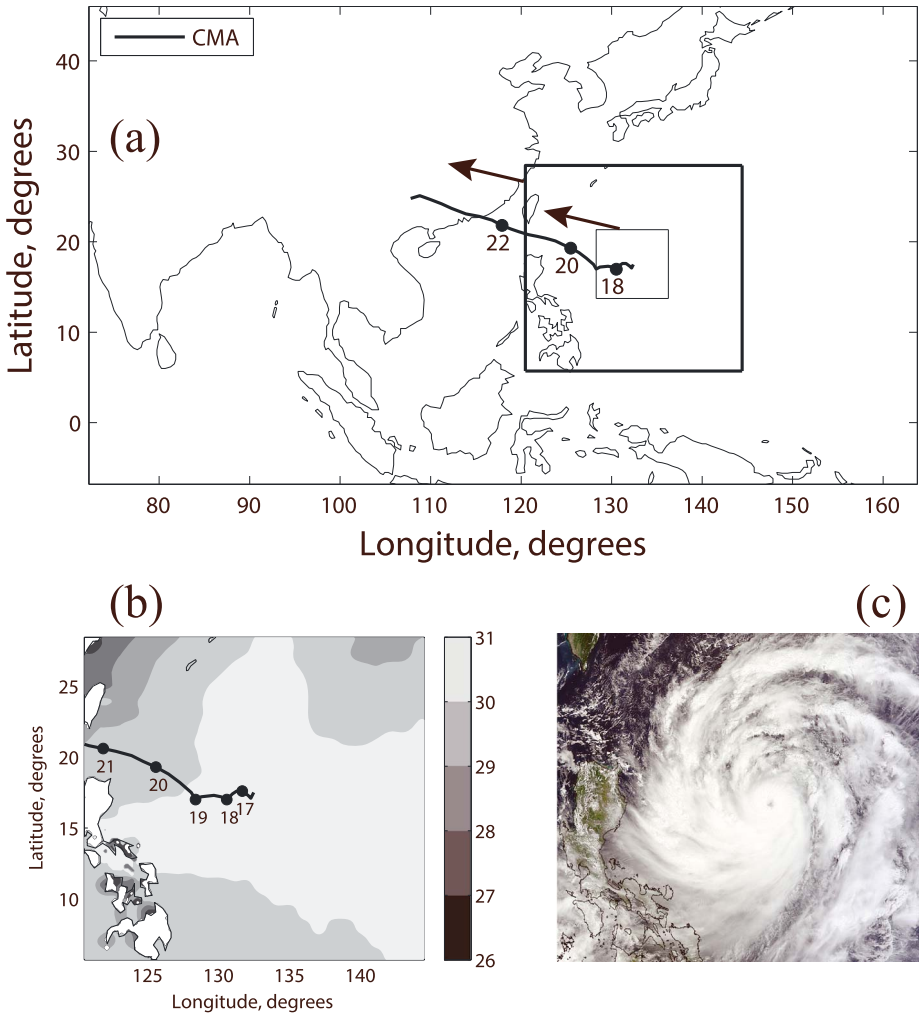

Figure 1. (a) The configurations of the model domains D1, D2, D3, and best track (black line) of Usagi (2013), from 0600 UTC 16 September to 0000 UTC 24 September according to the China Meteorological Administration (CMA). (b) The temperature of the sea surface (gray shading every 1°C) at 1200 UTC 16 September and CMA best track (black). All of the positions at 0000 UTC are marked with black dots, with their date provided above. (c) National Aeronautics and Space Administration (NASA) Moderate Resolution Imaging Spectroradiometer (MODIS) satellite visible image of Super Typhoon Usagi at 0225 UTC 19 September with a clear eyewall structure. Credit: NASA Goddard MODIS rapid response team.

We usually differentiate between external and internal factors that can impact the RI process of a TC. Statistical prediction models attempt to take advantage of the fact that a favorable enviroment is a necessity for RI, and forecast RI based on the values of large-scale environmental parameters, such as the vertical wind shear and sea surface temperature (Kaplan et al., 2010; Kaplan & DeMaria, 2003). However, many studies have shown that internal processes may also play an important role in RI, such as the initial intensity of the vortex and inner-core deep convection (e.g., Chang & Wu, 2017; Chen et al., 2017, 2018; Rogers et al., 2016; Wang & Wang, 2014; Zagrodnik & Jiang, 2014). Idealized simulations in a no-shear environment suggest that storms with stronger vortices undergo RI earlier (Miyamoto & Takemi, 2015). With respect to real-world cases, Munsell et al. (2017) found that a strong initial vortex can undergo RI regardless of unfavorable environmental conditions, such as when there is a strong vertical wind shear. Recent studies demonstrate that forecasting errors of TC intensity (including RI) are dominated by errors of the initial vortex intensity and inner-core moisture rather than environmental factors for the first 3–5 forecasting days (Emanuel & Zhang, 2016, 2017).

Tropospheric moisture has long been recognized as an important factor impacting TC intensification (Emanuel, 1989; Kaplan & DeMaria, 2003; Ooyama, 1969). Recently, more studies have focused on TC inner-core moisture. According to the definition in Emanuel and Zhang (2017), the term "inner-core" denotes the

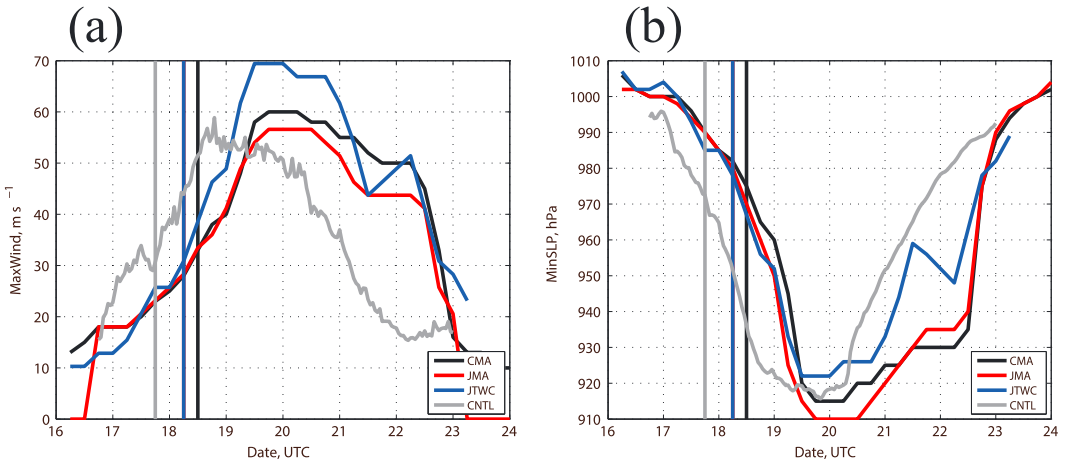

Figure 2. (a) The maximum surface wind speed from the best track estimate of Typhoon Usagi from the China Meteorological Administration (CMA; black), Japanese Meteorological Agency (JMA, red) and Joint Typhoon Warning Center (JTWC, blue). The control run forecast is also plotted in gray. (b) Same as (a) but for the minimum sea level pressure (hPa). Note that the maximum surface wind averaging windows used by CMA, JMA, and JTWC are 2, 10, and 1 min, respectively. The vertical lines indicate the rapid intensification (RI) onset timing in each case. The blue and red lines overlap because the JMA and JTWC best tracks have the same RI onset timings.

broad region of ascent in a TC, including the eyewall and the deep convection region outside it. Nolan (2007) found that the inner-core moisture of an idealized model in a no-shear and no-mean flow environment nearly becomes saturated at the onset of RI. Similarly, the idealized simulations by Emanuel and Zhang (2017) further showed that the error in the growth of the intensity is as sensitive to the initial inner-core moisture conditions as it is to the initial vortex intensity. High inner-core moisture contents induce deeper and more organized convection, thus increasing the TC intensity (Rios-Berrios et al., 2016). Moreover, observational studies (Nguyen et al., 2017; Zawislak et al., 2016) have indicated that the inner-core tropospheric dry air (especially in the up-shear quadrant) might hinder TC intensification in a sheared environment. Braun et al. (2012) suggested that dry air may only slow intensification processes down when located close to a vortex center during the early stages of TC development. They also showed that an asymmetric inner-core moisture deficit can slow down the intensification by inducing convective asymmetry. However, these studies on the impact of inner-core moisture either used idealized simulations or prescribed dry inner-core air. It is not clear how the errors in the inner-core moisture, which are small but still noticeable in real-world cases, can influence the onset of RI and evolution of the intensity.

In this study, we used the Pennsylvania State University (PSU) TC analysis and forecast system (PSU WRF-EnKF) to investigate TC Usagi (2013) with the Advanced Research Weather Research and Forecasting (WRF-ARW) model and an ensemble Kalman filter (EnKF) data assimilation method. We improved the modeling of the ICs of a TC vortex by assimilating satellite-derived atmosphere motion vectors (AMVs) into the model. AMVs are generated by tracking cloud and water vapor targets in sequential satellite images, which represent wind vectors at certain heights (Velden et al., 2005). Although AMVs can be affected by height assignment errors, analyses based on global models (Berger et al., 2011) and limited-area models (Velden et al., 2017) demonstrated that they have a positive impact on TC forecasts. AMVs are routinely produced by global operation centers and are available in global telecommunication system (GTS) data sets. Wu et al. (2014) showed that AMV data assimilation improves the accuracy of TC analysis and forecasting based on the WRF model and EnKF technique, particularly in track forecasting. The assimilation of AMVs yielded modest improvements in the results of TC intensity analysis and forecasting obtained using the convection-permitting simulation of the Hurricane WRF model (Velden et al., 2017). The impact was limited because the Hurricane WRF vortex relocation technique removed data-influenced increments from the core region. In this paper, we will examine the impact of assimilating AMVs into the convection-permitting WRF-ARW model and PSU WRF-EnKF system when analyzing and forecasting TC inner-core structure and intensity.

The goals of this study are twofold: (1) to show the benefit of assimilating AMVs to improve the vortex structure and intensity and (2) to examine the factors associated with the ICs (especially TC vortex intensity and

inner-core moisture) impacting the RI of Usagi. The paper is organized as follows: In section 2, we describe the experimental design and data set to be assimilated; we present the EnKF analysis increments and deterministic forecasts in terms of track and intensity in section 3; section 4 uses ensemble sensitivity analyses to examine key factors impacting RI onset timing; we outline sensitivity experiments to illustrate the impact of the initial inner-core moisture on the RI process in section 5; finally, we present our concluding remarks in section 6.

2. Methodology

The intensity estimations of Usagi by different monitoring agencies have large uncertainties (Figures 2a and 2b). Nevertheless, all agencies estimated similar minSLPs during the RI stage of the storm. Due to the lack of in situ observations in the west North Pacific region, the minSLP of Usagi, which was derived by a satellite-based Dvorak technique, may be a more reliable metric of Usagi's intensity than the wind speed. The minSLP of a TC is estimated directly from cloud pattern analysis (Ying et al., 2014). Therefore, we adopted the minSLP as the measure of Usagi's intensity. The minSLP and track data used in this study were obtained from the China Meteorological Administration. Furthermore, similarly to Munsell et al. (2017), we defined the RI onset timing as the time of the maximum change in intensity over the subsequent 24 hr (measured by minSLP). The current definition is sufficient to differentiate the RI onset timing of each simulation since the time difference (sequence) of the RI onset is the one that is used in the correlation analysis in section 4.

2.1. WRF and EnKF

We used the PSU WRF-EnKF TC analysis and prediction system (Weng & Zhang, 2016; Zhang et al., 2009) in this study, with a convection-permitting simulation of WRF-ARW model 3.6.1. We used three two-way nested domains (Figure 1a) with 61 vertical levels and a model top of 10 hPa. We used 379 × 244, 298 × 298, and 298 × 298 grid points with respective grid spacings of 27, 9, and 3 km in domains D1, D2, and D3 (Figure 1a). We only applied the modified Tiedtke cumulus scheme (Zhang et al., 2011) to the outermost domain (D1). We applied the WSM 6-class graupel scheme (Hong et al., 2004), the thermal diffusion scheme for land surfaces (Dudhia, 1996), and the Yonsei University scheme (Noh et al., 2003) for planetary boundary layer processes.

We obtained the initial and boundary conditions from 1 × 1 degree and 6-hourly final analysis of the global forecast system from the National Centers for Environmental Prediction. We conducted data assimilation independently for each domain. Note that we only assimilated data within the limited region (domain D2 region) because we replaced the TC environment (>800 km) with the global forecast system analysis every 6 hr. We applied the covariance relaxation method (Zhang et al., 2004) with a coefficient of 0.75. The horizontal localization radius of influence for AMVs is 100 km without vertical localization. We did not adopt any artificial vortex initialization (e.g., bogus vortex) or relocation schemes.

2.2. Data Set

We assimilated the GTS data and the TC position index (TPI; minSLP) every 3 hr. The TPI contained the best track minSLP information and was treated as a single point pressure observation. Since we focused on the development stage of Usagi, which occurred in Open Ocean, AMVs are the most common available data. We used AMVs generated by the visible and water vapor channels of the Japanese Multifunctional Transport Satellite-2. We reduced the resolution of the AMVs before assimilation because assimilating the high resolution AMVs may increase computing costs and invalidate the assumption that the observation errors are spatially independent.

2.3. Experimental Design

As shown in the flowchart in Figure 3, the initial ensemble was generated at 1200 UTC 16 September using the National Centers for Environmental Prediction final analysis. The initial perturbations were generated by the WRF data assimilation system (WRFDA; version 3.6) with the "CV5" background error covariance option (Barker et al., 2004). The background error covariance matrix of domain D1 was calculated from a set of monthlong 12-hr forecasts minus 24-hr forecasts according to the National Meteorological Center method (Parrish & Derber, 1992). First, we integrated the ensemble for 6 hr so that flow-dependent covariance structures could develop. Then, starting at 1800 UTC 16 September, we assimilated the GTS and TPI data every 3 hr for 1 day until 1800 UTC 17 September. The CNTL was integrated from 1800 UTC 16 September up to the time

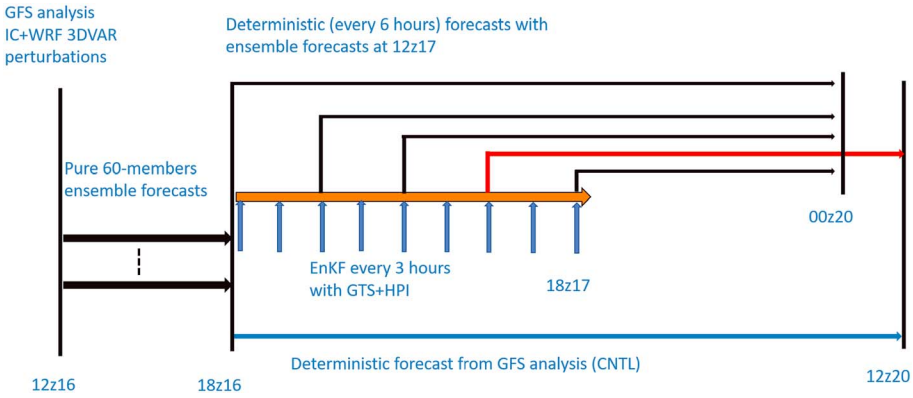

Figure 3. A schematic flowchart of the ensemble Kalman filter (EnKF) and control run (CNTL) experiments. The thick blue arrow from 1800 UTC 16 to 1200 UTC 20 September represents the CNTL simulation with the global forecast system initial condition. The small orange vertical arrows between 1800 UTC 16 and 1800 UTC 17 September represent the EnKF cycling at 3-hr intervals. The thin black arrows between the EnKF cycles and 0000 UTC 20 September indicate the deterministic forecasts initialized from the EnKF analysis. The thin red arrow between 1200 UTC 17 and 1200 UTC 20 September represents the ensemble forecasts initialized from the EnKF analysis ensemble.

that the storm weakened into a tropical depression. We initiated deterministic forecasts every 6 hr from the EnKF analysis and simulated them until the end of the intensification process at 0000 UTC 20 September. We used the EnKF analysis ensemble at 1200 UTC 17 September as the ICs for the convection-permitting ensemble forecasts, which we simulated for 72 hr, that is, up until the end of the intensification stage at 1200 UTC 20 September.

3. Data Assimilation and Deterministic Forecasts

3.1. Control Run

As mentioned in the introduction, the CNTL model surprisingly predicted that Usagi would intensify earlier than observed, forecasting the RI onset 18 hr earlier than that of the best track (Figure 2). Due to this displacement of the RI onset, CNTL predicted the intensity (minSLP) to be much stronger than the best track, disagreeing by up to 40 hPa at 0000 UTC 19 September (Figure 2b). The simulations initialized from other times (e.g., every 6 hr between 0600 UTC 17 and 1800 UTC 17, not shown) also predicted early RI onset times.

3.2. Track and Intensity of Deterministic Forecasts

While assimilating AMVs, consecutive deterministic forecasts are initiated every 6 hr from the EnKF analysis, as shown in Figure 4a. Compared to the CNTL, the RI onset timings predicted by these deterministic forecasts progressively improved, and hence, the minSLP errors decreased (Figure 4c). The two best deterministic forecasts, initiated at 1200 and 1800 UTC 17 September, were much closer in intensity to the best track, although they were still slightly stronger. Compared to the CNTL, the simulation initialized at 0000 UTC 19 September reduced the minSLP errors by more than a half, as shown in Figure 4c. The track forecasts improved marginally because the track of this storm was controlled by the stable WNPSH.

3.3. EnKF Analysis Increments

The AMVs were assimilated every 3 hr, as shown in Figure 3. All data within domain D2 are shown in Figure 4d. Although the majority of AMVs were above 250 hPa, about 40% were below 400 hPa. A significant percentage of AMVs were close to the center of the storm, as shown in Figure 4d. The top panels in Figure 5 illustrate the azimuthally averaged tangential/radial wind speeds according to the prior (EnKF input), analysis (EnKF output), and their increments in the first EnKF cycle, when Usagi was still a weak tropical storm. At this time, a moderate-weak vortex in the EnKF prior had a 15 m s^{-1} maximum tangential wind speed at a 200-km radius from the surface center. After the first EnKF cycle, the tangential wind speed incremented negatively (around 2 m s^{-1}) throughout the entire troposphere following the assimilation of AMVs (Figure 5c). The EnKF analysis predicted the radius of the V_{max} to be further away from the surface center than the EnKF prior. Both the

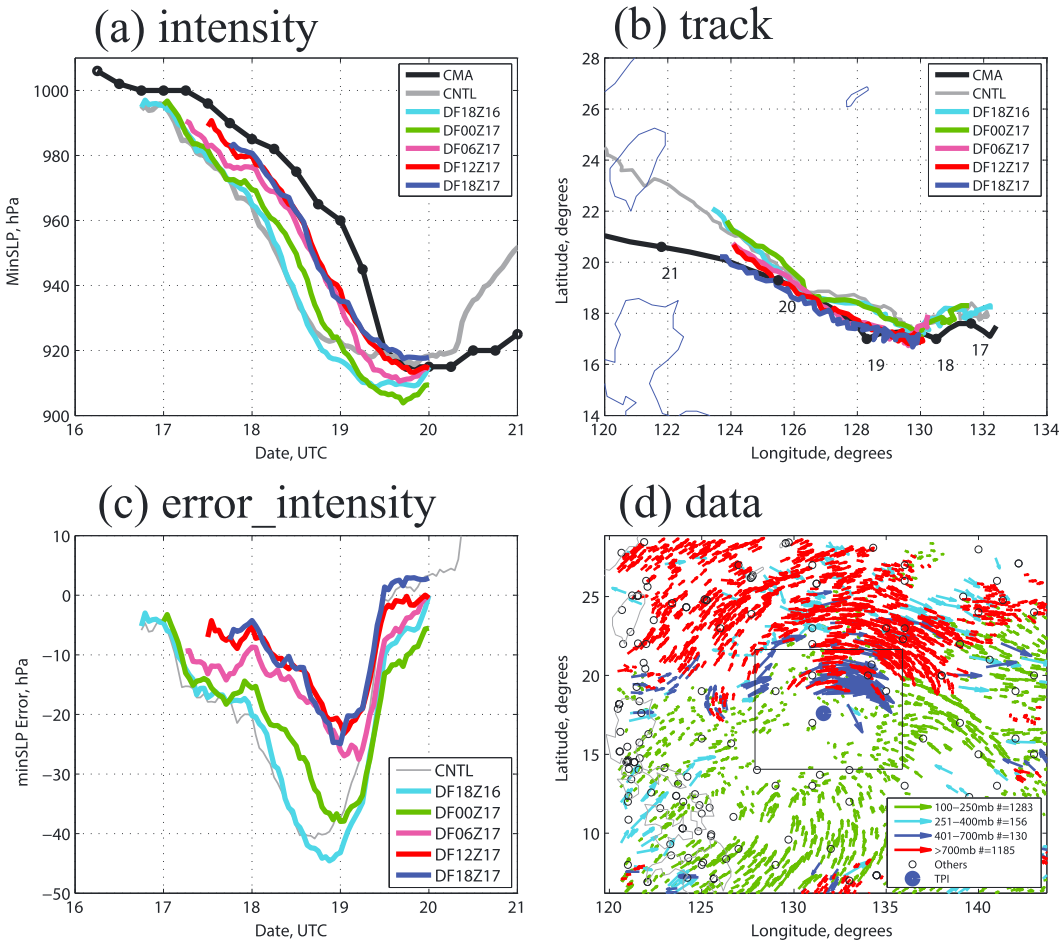

Figure 4. Evolution of (a) minimum sea level pressure (minSLP), (b) track, and (c) error minSLP according to deterministic forecasts initialized from the ensemble Kalman filter analysis. The best track from the China Meteorological Administration is plotted in black. (d) Distribution of the global telecommunication system data set and tropical cyclone position index at 0000 UTC 17 September within the domain 2 range. The atmospheric motion vectors are grouped by height into four layers (100–250, 251–400, 401–700, and >700 mb) and indicated with different colors, and with numbers to show the total data points in each layer. The location of domain 3 is represented by the rectangular box.

primary and secondary circulations were modified. The boundary layer radial inflow decreased by around 10% and the upper level outflow decreased by 30% (Figure 5c). At 0900 UTC 17 September, the vortex became stronger and more compact after five EnKF cycles (15 hr; Figure 5d), while both the primary and secondary circulations weakened with increments of the EnKF analysis, particularly within the inner-core of the TC, as indicated in Figure 5f. After 24 hr, the ensemble mean vortex intensity is considerably weaker (10 hPa higher in minSLP) than that of the CNTL without the AMV assimilation. For the last two cycles (1500 and 1800 UTC 17 September), the increments become rather insignificant (not shown). This explains the negligible improvement on TC intensity forecasts between deterministic forecasts initialized at 1200 and 1800 UTC 17 September. We believe that correcting the vortex strength (intensity) systematically improves the deterministic forecasts. We will demonstrate further evidence for this in section 4, where we present the results of ensemble sensitivity analyses.

It is worth mentioning that other data may have also contributed to increments during the EnKF analysis. For example, assimilation of the TPI may contribute to the analysis increments in the lower troposphere. However, as shown in Figures 5c and 5f, the negative increments in the tangential wind speed were throughout the troposphere, especially in the middle troposphere (5–6 km). The AMV data, which are available from the lower to upper troposphere, are the only data source that significantly contributed to the analysis across the entire troposphere.

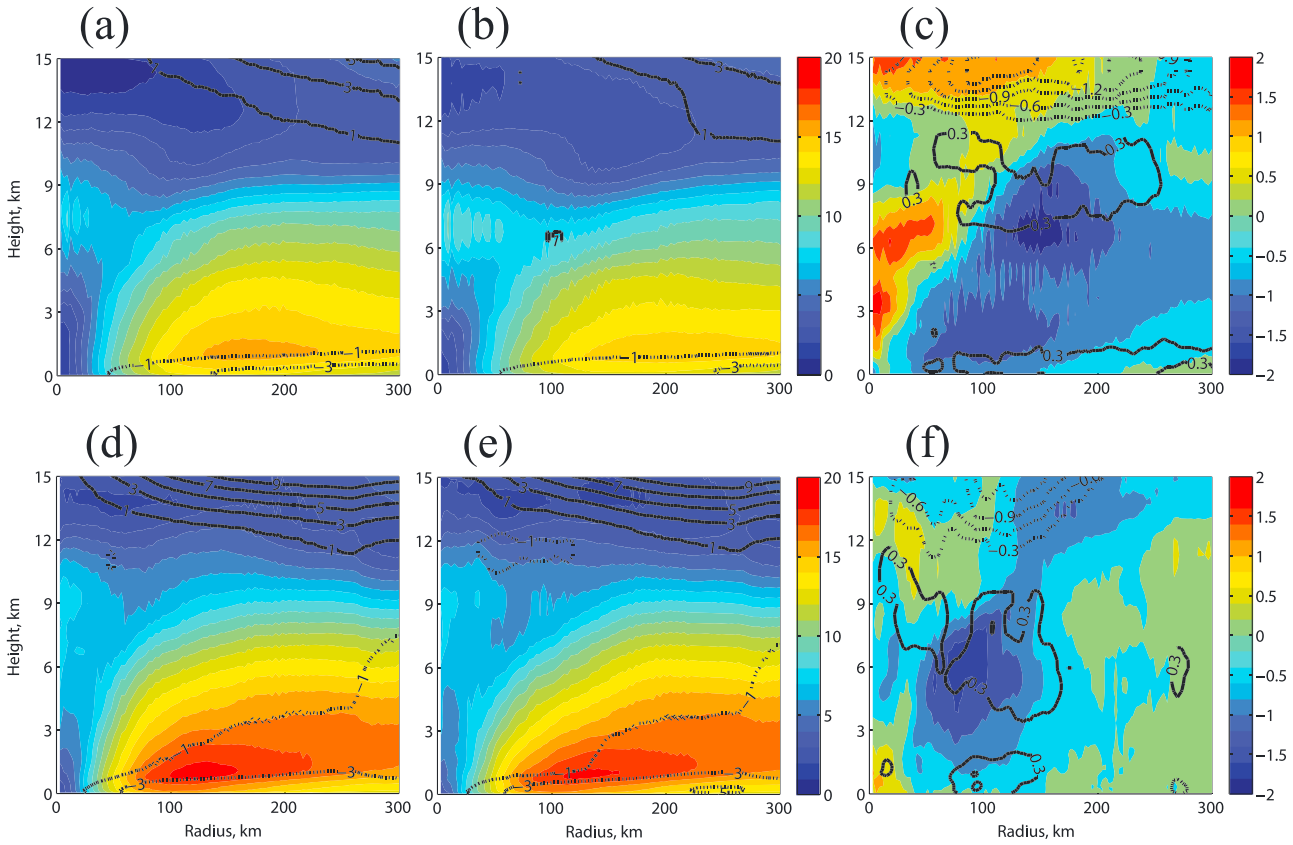

Figure 5. The azimuthal average tangential (shading) and radial (contour in 2 m s^{-1} interval) wind speeds of (a) ensemble Kalman filter (EnKF) prior, (b) EnKF analysis, and (c) EnKF increment at 1800 UTC 16 September (first EnKF cycle). (d–f) The equivalents to the top panels from 0900 UTC 17 September. The positive (negative) values are represented as solid (dot) contours in each figure.

It is also worth mentioning that there was a considerable spread of vortex vorticity across the ensemble, in both low and middle levels (not shown). The AMVs were beneficial, but not sufficient to constrain the vortex intensity. AMVs are limited by a relatively low coverage since it only can be generated at the edge of clouds. Furthermore, the EnKF algorithm propagates information between different variables, thus modifying other thermodynamic parameters (e.g., water vapor mixing ratio and hydrometeors). The deterministic forecasts from an additional experiment with a similar data assimilation setting, but without incrementing the water vapor mixing ratio (Qvapor) or any of the hydrometeors fields (all six species in WSM6 scheme), presented a similar evolution (not shown). This suggests the limited ability of assimilating AMVs to improve the moisture field in this Usagi case.

4. Ensemble Forecast and Sensitivity Analysis

In the previous section, we showed that data assimilation improved the structure and intensity of Super Typhoon Usagi (2013). We studied the dynamics and predictability of the Usagi RI process with a 60-member convection-permitting ensemble simulation initialized from the EnKF analysis ensemble. The initial intensities of the ensemble varied from 995 to 980 hPa at 1200 UTC 17 September (Figure 6b). We integrated each member of the ensemble for 72 hr, until the end of the intensification stage. Figures 6a and 6b show each member colored by its RI onset timing. The stable steering flow, which was controlled by WNPSH, narrowly distributed the tracks of the ensemble members close to the best track. Every member of the ensemble intensified rapidly under moderate-weak wind shear conditions (Figure 6c) and over extremely warm ocean surfaces, with 15 members comparable to the best track intensity in terms of the minSLP evolution. However, there was a significant spread in the RI onset timing (as large as 35 hr) and a huge spread in the intensity (e.g., 60 hPa at 0000 UTC 19 September) between individual members of the ensemble. These findings

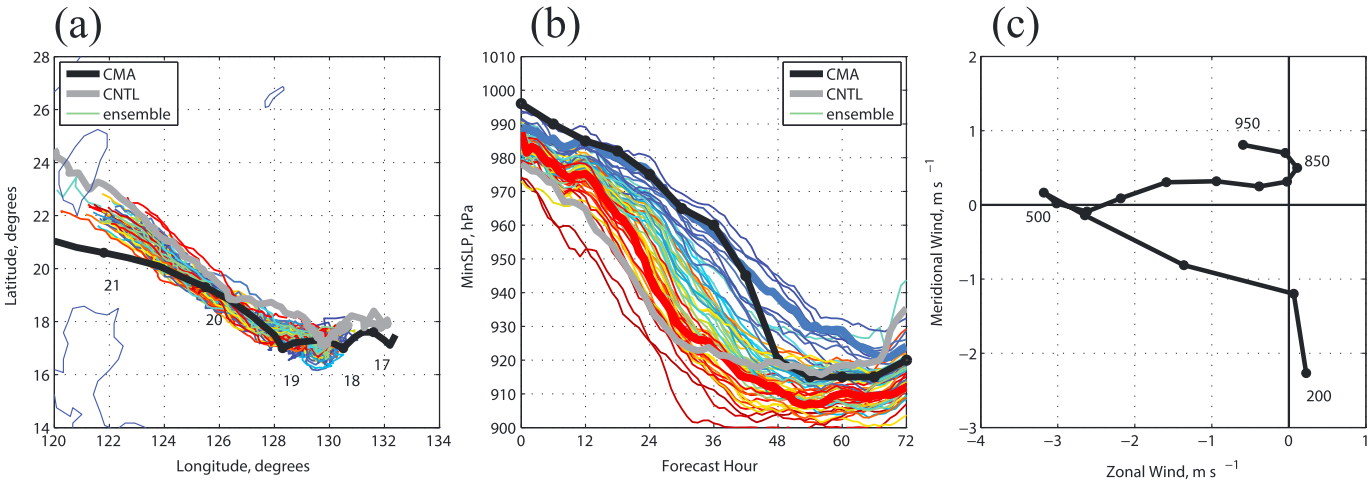

Figure 6. Evolution of (a) track and (b) minimum sea level pressure of ensemble and control run experiments. The China Meteorological Administration best track is plotted in black. Each member is colored corresponding to its rapid intensification (RI) onset timing. Early RI members have warmer colors, while late members have cooler colors. The two thick lines correspond to two representative weak and strong simulations. The 60-member ensemble forecasts are initialized at 1200 UTC 17 September. (c) Composite hodograph from the ensemble at the initial time. The dots represent area-averaged winds within an annulus of 200–800 km from the surface center extending from 950 to 200 hPa (every 50 hPa).

motivated us to investigate the predictability associated with the governing dynamics of the RI process. It is worth mentioning that the intensity forecasts from the EnKF analysis ensemble were slightly biased toward stronger intensities. Every member had a deeper minSLP than the best track, which we believed to be caused in part by the mean bias in the initial vortex intensity (also shown in Figure 6b) and/or the uncertainty of the model physics.

4.1. Ensemble RI-Onset Variability: Impacts of Shear and Tilt

Environmental factors can strongly influence TC intensification processes. For example, vertical wind shear can strongly impact the RI process by modulating the TC vortex tilt (Tao & Zhang, 2014; Zhang & Tao, 2013). Convection is typically enhanced on the down-shear side but suppressed on the up-shear side. A sheared TC can evolve under the influence of two processes, namely, precession and alignment (Rappin & Nolan, 2012; Tao & Zhang, 2015). During the precession stage, the TC tilt vector rotates cyclonically and gradually decreases. RI typically begins right after alignment, that is, when the magnitude of the tilt vector is small (Miyamoto & Nolan, 2018; Munsell et al., 2017; Rogers et al., 2016). The ensemble forecasts started under moderate-weak shear conditions, with an ensemble mean deep layer shear of 4 m s^{-1} (Figure 6c). We calculated the deep layer shear by taking the difference between 850 and 200 hPa and averaging the wind speed over a 200–800 km annulus. At later times, the shear slightly increased in magnitude, to 6–8 m s^{-1}, then decreased to 4 m s^{-1} in all members (not shown). These shear magnitudes are considered moderate to small.

We calculated the tilt vector by measuring the difference between the midlevel (500 hPa) and low-level (850 hPa) circulation centers, which were determined by finding the point such that the summation of the inner-core tangential wind was maximized. This method is particularly helpful for tracking weak vortices. As shown in Figure 7a, some members, with both early and late intensification, had quite large initial tilt magnitudes due to the moderate-weak environmental shear. The entire ensemble exhibited rapidly decreasing tilt magnitudes after the model initialization, being smaller than 40 km at the RI onset (Figure 7a), which is consistent with the findings in Munsell et al. (2017). It should be noted that RI did not always occur immediately after the vortex tilt magnitude decreased significantly (Figure 7c). Thus, a small tilt magnitude is necessary for RI onset but may not be sufficient.

4.2. Ensemble RI-Onset Variability: Impacts of Initial Vortex Strength

Previous studies show that a stronger initial vortex is more likely to intensify quickly, regardless certain unfavorable environmental conditions (Emanuel & Zhang, 2016; Munsell et al., 2013, 2017; Torn & Cook, 2013; Zhang & Emanuel, 2016). This was also the case in the ensemble simulations of Usagi (Figure 6b). The

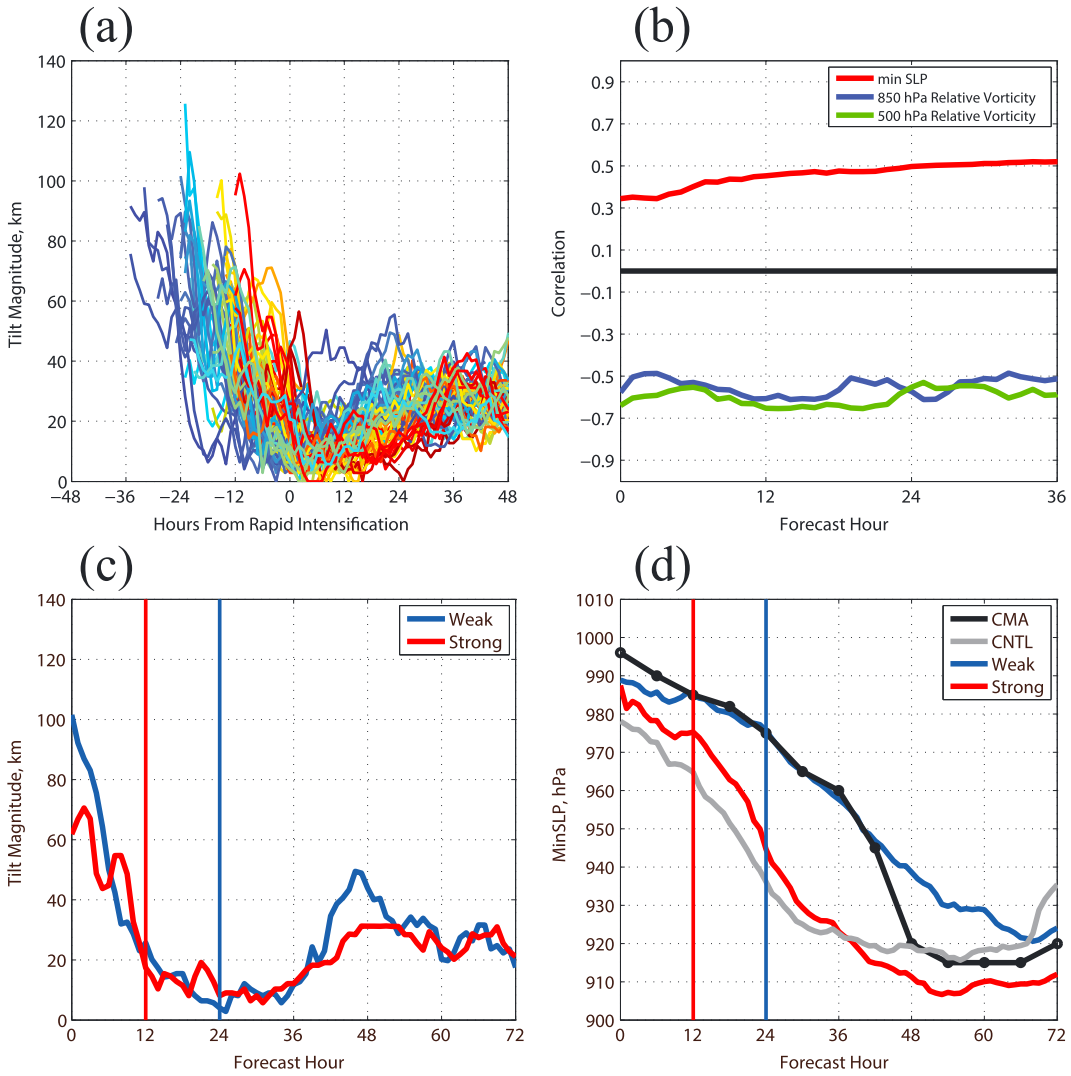

Figure 7. (a) Evolution of the tilt magnitudes (the distance between the circulation centers at 850 and 500 hPa) using the rapid intensification (RI) onset timing as a reference time (0 hr). (b) Evolution of the correlations between the area-averaged (within 200-km radius of the surface center) vorticity (500 and 850 hPa) and the RI onset timing and between the minimum sea level pressure (minSLP) and the RI onset timing. All correlations satisfied the 99% confidence level. (c) Evolution of the tilt magnitudes of two representative members: one weak and one strong. (d) Evolution of the minSLP of the weak, strong, and control run simulations. The China Meteorological Administration best track is plotted in black. The red (blue) vertical lines at (c) and (d) represent the RI onset timing of the strong (weak) simulation.

strong members (warm colors) tended to be strong throughout the simulation. The correlation between the initial minSLP and the RI onset time started at 0.3 and increased to around 0.5, until all members started RI (Figure 7b), which occurred within 36 hr. We also calculated the low-level (850 hPa) and midlevel (500 hPa) relative vorticity by averaging the vorticity within a 200-km radius of the circulation center on each level. The correlations, all of which satisfied the 99% confidence level, between the low and midlevel relative vorticity and the RI onset timing were maintained at approximately −0.5. The correlations between the RI onset timing and the vorticity/minSLP suggest that the variance in the RI onset timing can be partially explained by the differences in initial intensity between the vortices. This finding also explains why assimilating AMVs benefits the forecasting of Usagi's RI process, as discussed in section 3. Assimilating AMVs progressively improved the ICs of the deterministic forecasts by improving the initial vortex intensity and thus postponed the predicted RI onset time.

However, ensemble members sharing similar initial intensities and tilt evolutions differed significantly in terms of their RI onset timing and intensity, as shown in Figures 7c and 7d. The forecasted intensity and

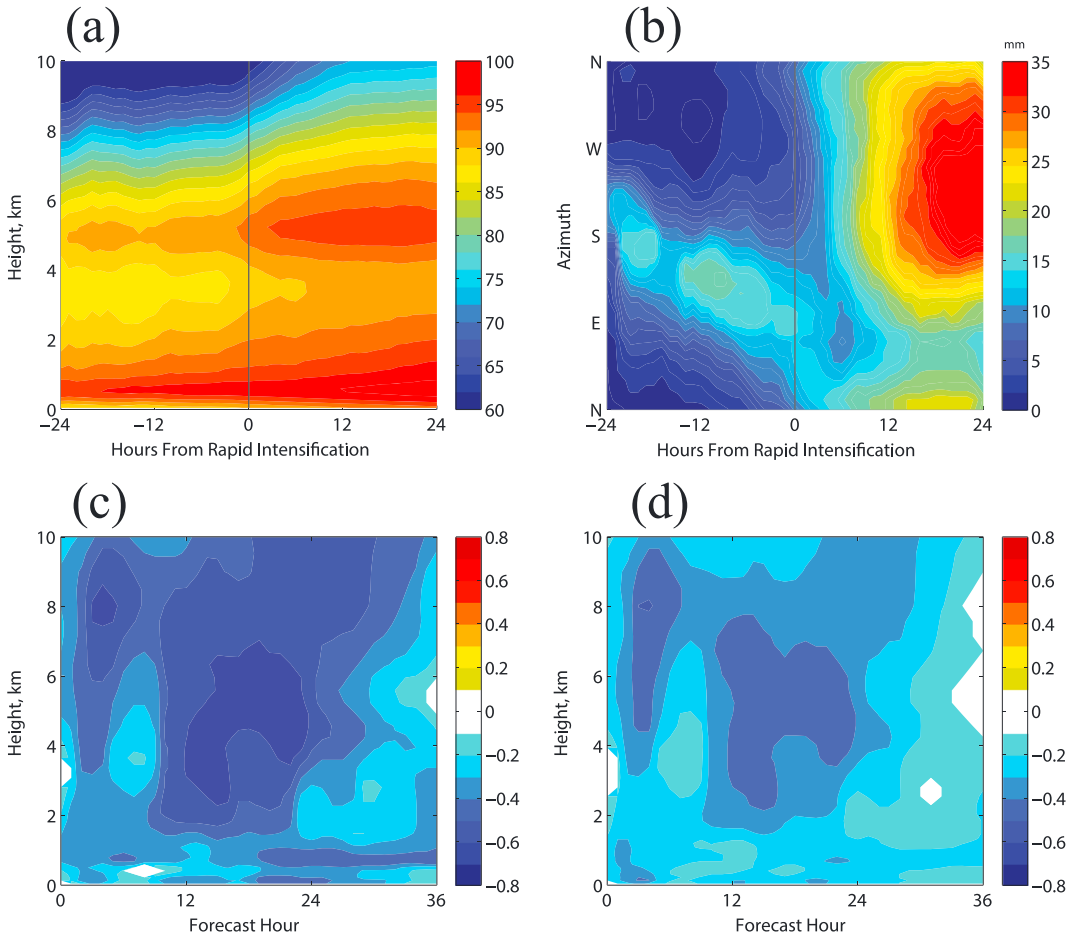

Figure 8. (a) Height-time plot of the inner-core relative humidity (RH) over a 150-km radius. (b) Azimuth-time plot of the precipitation averaged over a 50-km radius. Both (a) and (b) use the rapid intensification (RI) onset timing as a reference time (0 hr). (c) Height-time plot of the correlation between the RH (area averaged over a 150-km radius) and RI onset timing. (d) Height-time plot of the partial correlation between the RH and the RI onset timing, controlling the current vortex intensity (minimum sea level pressure) as a constant.

the spread of timing of RI onset times can only be partially explained by the initial intensity differences. As mentioned in the introduction, many studies have reported the importance of inner-core moisture for RI onset. Therefore, we analyzed the effect of varying the inner-core moisture contents on Usagi's RI process in detail in sections 4.3, 4.4, and 5.

4.3. Ensemble RI-Onset Variability: Impacts of Inner-Core Moisture

Using the RI onset as a reference time, the evolution of the ensemble mean vertical profile of the inner-core relative humidity (RH) is shown in Figure 8a. The RH of the entire column increased steadily before the storm progressed RI, exceeding 88% up to 6.5 km before the RI onset. The midlevel RH increased abruptly because the convection lifted the moisture above the freezing level. This finding is consistent with the results reported by earlier modeling studies (Emanuel, 1989; Kieu et al., 2014; Pauluis & Held, 2002) and observation studies (Rogers et al., 2016; Zawislak et al., 2016).

The ensemble-mean azimuth-time evolution of the area-averaged precipitation within a 50-km radius, which provides an indication of the strength of the inner-core convection, is plotted with respect to the RI onset in Figure 8b. The strong convection is located on the south side of the vortex due to the moderate-weak north-easterly shear at the beginning of the simulation (Figure 6c). Subsequently, the convection propagated cyclonically to the up-shear quadrant and became markedly more axisymmetric by the time of the RI onset. This is consistent with the Tropical Rainfall Measuring Mission observations of Super Typhoon Usagi (NASA, 2013).

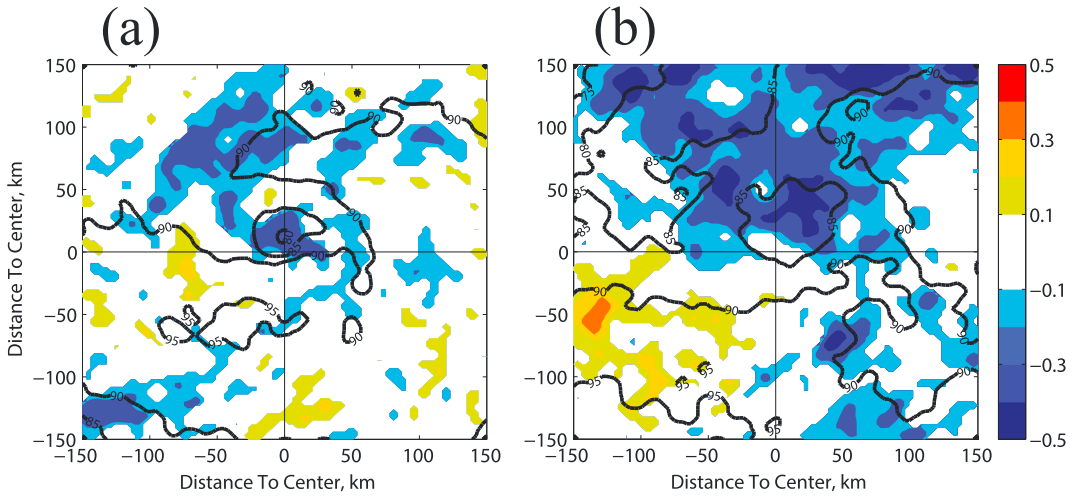

Figure 9. Partial correlation between the relative humidity (RH) of the initial ensemble and the rapid intensification onset timing at (a) 850 hPa and (b) 500 hPa, while holding the initial intensity (minimum sea level pressure) constant. The contours indicate the ensemble mean RH field.

Some observational studies (Harnos & Nesbitt, 2011; Jiang, 2012; Kieper & Jiang, 2012; Rogers et al., 2015, 2016; Stevenson et al., 2014; Zagrodnik & Jiang, 2014; Zawislak et al., 2016) and modeling studies (Chen et al., 2017; Chen & Gopalakrishnan, 2015; Leighton et al., 2018; Miyamoto & Takemi, 2013; Munsell et al., 2017; Onderlinde & Nolan, 2014, 2016) found similar convection propagation and axisymmetrization under vertical wind shear.

Figure 8c shows the evolution of the correlation between the area-averaged RH within a 150-km radius and the RI onset timing of the 60-member ensemble at each height. A negative correlation indicates that RI begins earlier when moisture is more abundant (higher RH). There were moderate correlations (−0.5 to −0.7) during 0–24 hr and from low levels to a height of around 10 km. Partial correlations between RH and the RI onset timing are shown in Figure 8d. We applied partial correlations so that we could clarify relationships when multiple variables were all correlated with each other. We separated the effect of the current vortex intensity from the statistical relationships targeted by our analysis, by taking the partial correlation between the RH and the RI onset timing while controlling a third variable (current vortex intensity, represented by minSLP), effectively treating it as a constant (Sippel & Zhang, 2010). The partial correlation varied in a similar manner to the variation shown in Figure 8c but had larger negative values. There were moderate partial correlations throughout the troposphere at the initial time of the simulation (−0.3 to −0.5). Strong correlations are found at midlevels (4–7 km) between 12 and 24 hr (Figure 8a). In general, the evolution of the deep layer moisture contents and correlation analyses provide clear evidences that the inner-core tropospheric moisture conditions affect the RI timing in this ensemble.

We narrowed down our focus on the impact of the initial moisture conditions because of their critical influence on the strength and location of convection. The partial correlations between the initial moisture (RH) and RI onset time are shown in Figure 9. At 850 hPa (Figure 9a), we detected moderately weak partial correlations (−0.3 to −0.5) between the moisture and the RI onset timing up to 100 km to the northwest and southwest of the center of the storm. Meanwhile, there was a larger area with negative correlations at 500 hPa, mostly to the north of the storm (Figure 9b). The RI would have begun earlier if there had been a greater abundance of moisture in this area. We interpreted these negative correlations as indicating the importance of the midlevel moisture to the north of the storm in determining the RI onset timing. There were almost no significant correlations outside the inner-core region (not shown). The correlations between the RI onset timing and the initial moisture field indicate that we can attribute some of the variation in the RI onset timing to the initial inner-core moisture conditions in addition to the initial intensity.

4.4. Impacts of Initial Inner-Core Moisture: Examples From Two Contrasting Members

We analyzed the effect of the inner-core moisture on the RI onset timing in further detail by selecting one weak simulation of the ensemble (denoted as Weak because of its weak TC intensity among ensemble

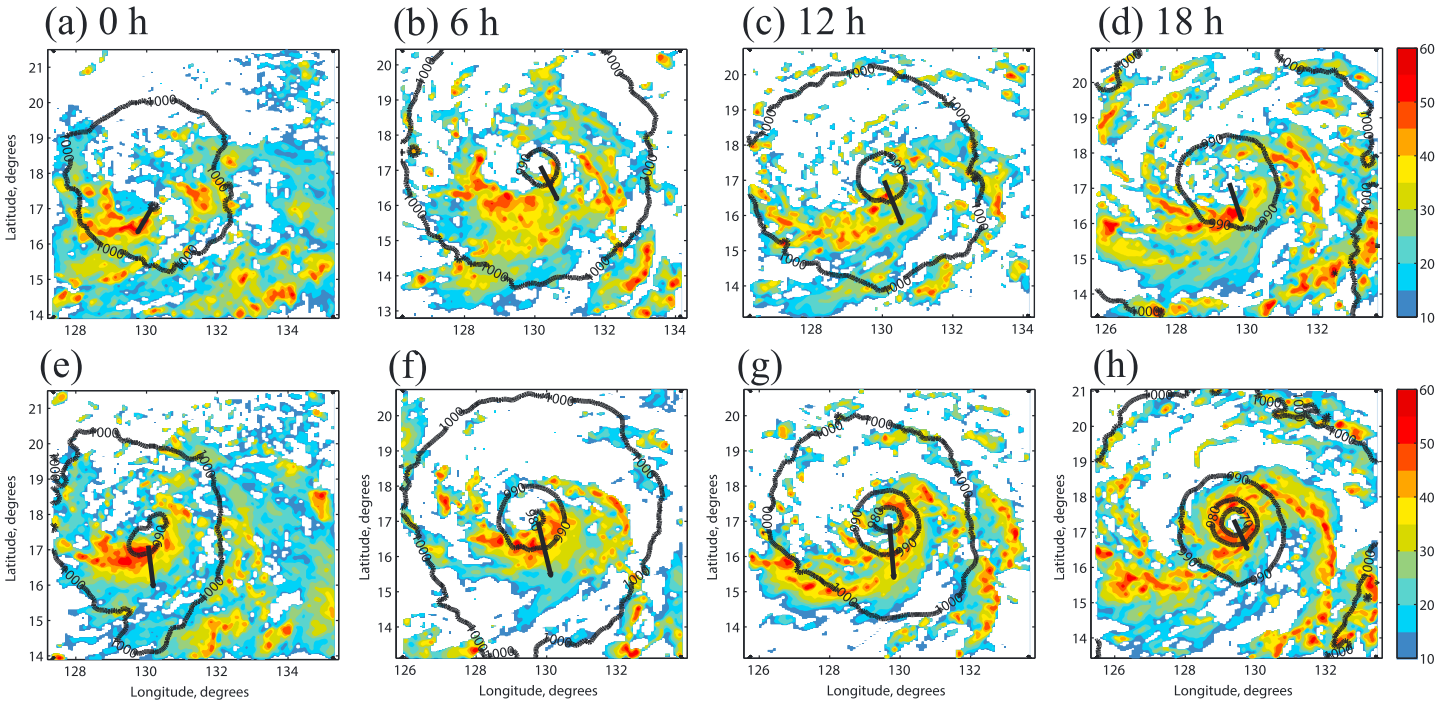

Figure 10. Composite reflectivity (shading; every 5 dBZ) of (a–d) Weak and (e–h) Strong simulations. The sea level pressure (contour, every 10-hPa interval) and deep layer shear (black vector, 850–200 hPa; area-averaged over a 200–800 km annulus) are also plotted. (a and e) 0 hr; (b and f) 6 hr; (c and g) 12 hr; (d and h) 18 hr.

members), which agreed with the best track intensity reasonably well, and one strong simulation (denoted as Strong). These allowed us to illustrate the impact of moisture conditions on the TC intensification process. Despite their similar initial intensities and tilt evolutions (Figure 7c), the Strong simulation started RI 12 hr before the Weak simulation (Figure 7d). The vortex intensities of these two simulations diverged dramatically, differing by 40 hPa at 36 hr. Among all the members, these two simulations show the largest differences in the RI onset timing and the forecasted intensity evolution with a small initial intensity difference. Thus, we expected to discover useful information about the influence of the moisture field on the intensification process by comparing these two simulations since composites remove important details.

We studied the evolution of the convection to gain a more detailed understanding of these two simulations (Figure 10). The evolutions of the convection associated with the intensification of the Strong and Weak simulations can be differentiated according to their distinct properties. Both simulations initially contained regions of simulated radar reflectivity exceeding 40 dBZ, representing vigorous convection. The initial 4 m s^{-1} northeasterly shear, which is considered moderate-weak, caused the maximum value of the reflectivity to occur to the south of the center of the surface (down-shear quadrant). At 6 hr, active convection in the Strong simulation moves closer to the surface center (Figure 10f). At 12 hr, the Strong simulation has high reflectivity developing on the up-shear quadrant and active convection starts to wrap around the surface center (Figure 10g). The RI process began immediately after axisymmetrization of the convection. By 18 hr, the convection had already surrounded the center of the surface, which featured a noticeable axisymmetric eyewall structure, as illustrated in Figure 10h. The evolution of the convection of the Strong simulation was consistent with the ensemble mean analysis in Figure 8b. In contrast, disorganized convection in the Weak simulation is trapped on the south side of the surface center (down-shear quadrant) for a long time. Eventually, the Weak simulation developed convection on the north side of the storm, wrapped around the center, and then initiated RI at 24 hr (not shown). RI initiates immediately after the axisymmetrization of convection, which is consistent with previous idealized simulations (e.g., Miyamoto & Takemi, 2013; Tao & Zhang, 2015).

We conducted further analysis of these two simulations by investigating the evolution of their moisture fields. To facilitate the comparison, we used the storm-centered differences. Up to 300 km north or west of the

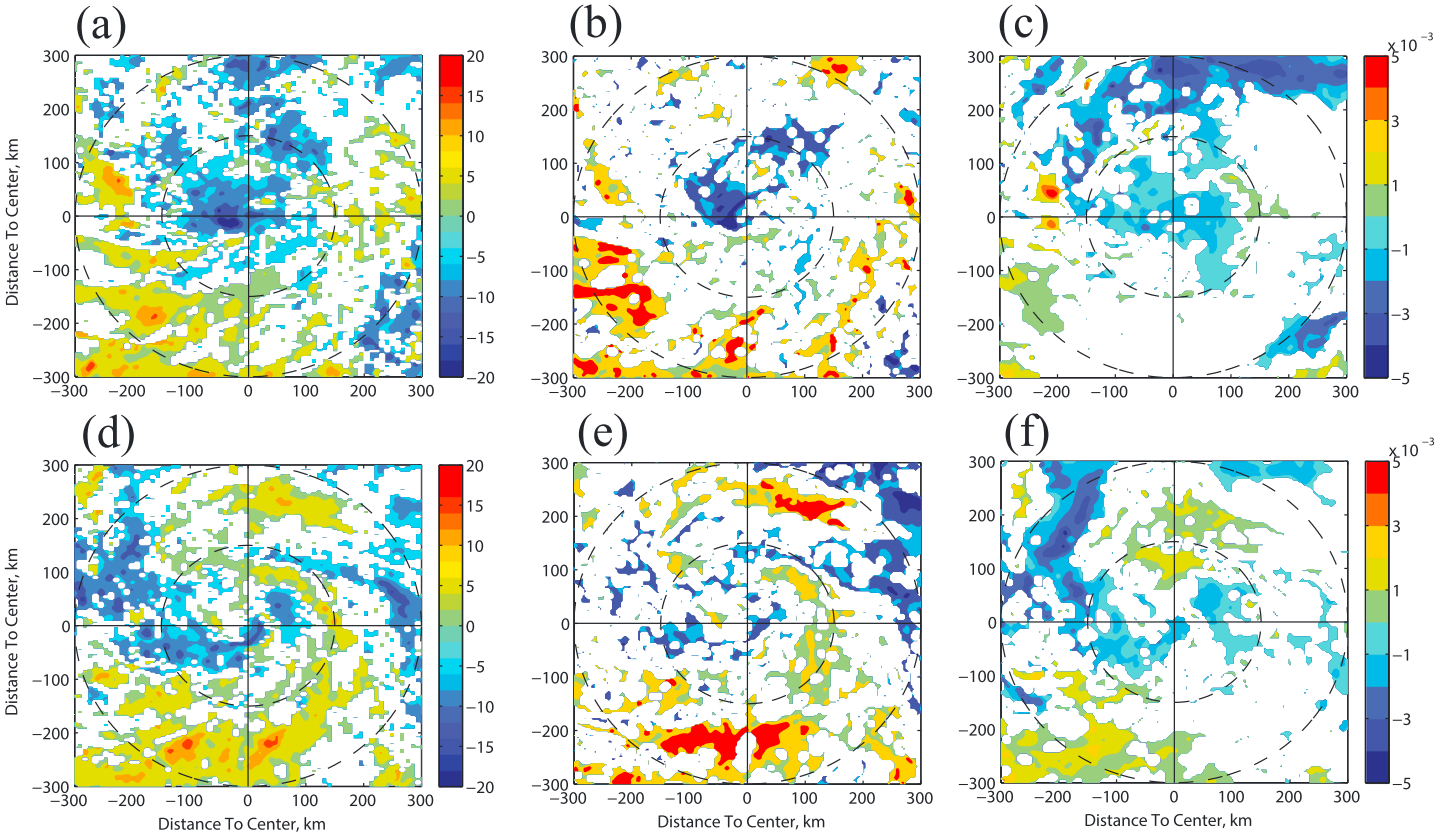

Figure 11. Differences between the Weak and Strong simulations at two forecast times: (a–c) 0 hr and (d–f) 6 hr. (a and d) Water vapor path; (b and e) Qvapor at 850 hPa; (c and f) Qvapor at 500 hPa. Only data with statistically significant differences ($>0.5\sigma$) are included. The two dashed circles indicate the 150- and 300-km radii.

surface center, the water vapor path of the Strong simulation was initially, at most, 20 mm greater than that of the Weak simulation, as shown in Figure 11a. Since water vapor path is a vertically integrated quantity, the Qvapor (water vapor mixing ratio) differences are further investigated at two vertical levels (850 and 500 hPa). At the lower level (850 hPa), the greatest Qvapor differences were north of the surface center, particularly within a 150-km radius (Figure 11b). Meanwhile, we observed similar differences to the north of the storm at 500 hPa but extended to a 300-km radius. After 6-hr integration, the air column with significant differences in water vapor path moves to the west of the center. Figure 11f shows that similar features were more prominent at 500 hPa, where drier midlevel air that was originally from the northern region of the Weak simulation rotated cyclonically to the west, also migrated inward to the center. However, the Qvapor differences become trivial at 850 hPa. Emanuel (1989) reported that the low-level moisture deficit could be recovered by sea-surface flux.

Overall, there were similar moisture contents to the south and east of these two simulations, which was mainly due to prior establishment of the convection (Figure 10). The Strong simulation contained more moisture to its north, which is the region that was indicated to exhibit high (negative) correlations in Figure 9. These high correlations suggest that the moisture in this region plays an important role in enhancing the inner-core convection and subsequently contributes to the axisymmetrization process in the Strong simulation, which is critical to RI onset. The drier air in the north of the Weak simulation may have weakened the inner-core convection and thus postponed the axisymmetrization.

5. Role of Initial Inner-Core Moisture: Sensitivity Experiments

Previous results have suggested that differences in initial inner-core moisture content affect the variation in RI onset timing and vortex intensity by modulating convection. We conducted two sensitivity experiments to

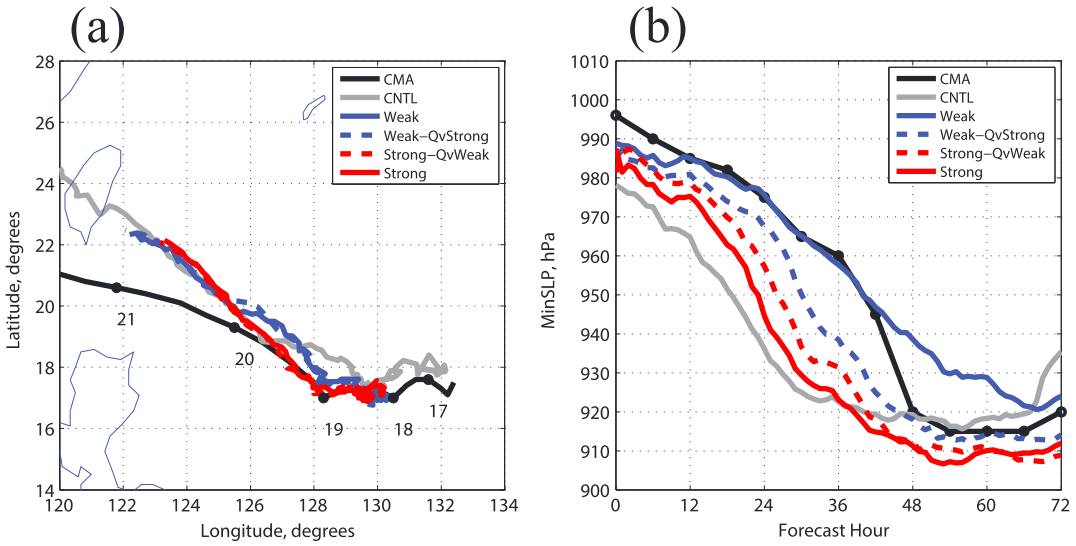

Figure 12. Evolution of (a) track and (b) minimum sea level pressure for five simulations: Weak, Weak-QvStrong, Strong-QvWeak, Strong, and control run. The China Meteorological Administration best track is plotted in black.

investigate the forecasted RI onset and intensity with respect to the ICs, specifically the moisture content of the inner-core troposphere. We set up these two simulations (Weak-QvStrong and Strong-QvWeak) by switching the Qvapor field within a 300-km radius of the storm surface center while holding all of the other fields the same. We selected a radius of 300 km so that we could focus on the impact of moisture within the active convection region (the broad concept of inner core defined in Emanuel & Zhang, 2017).

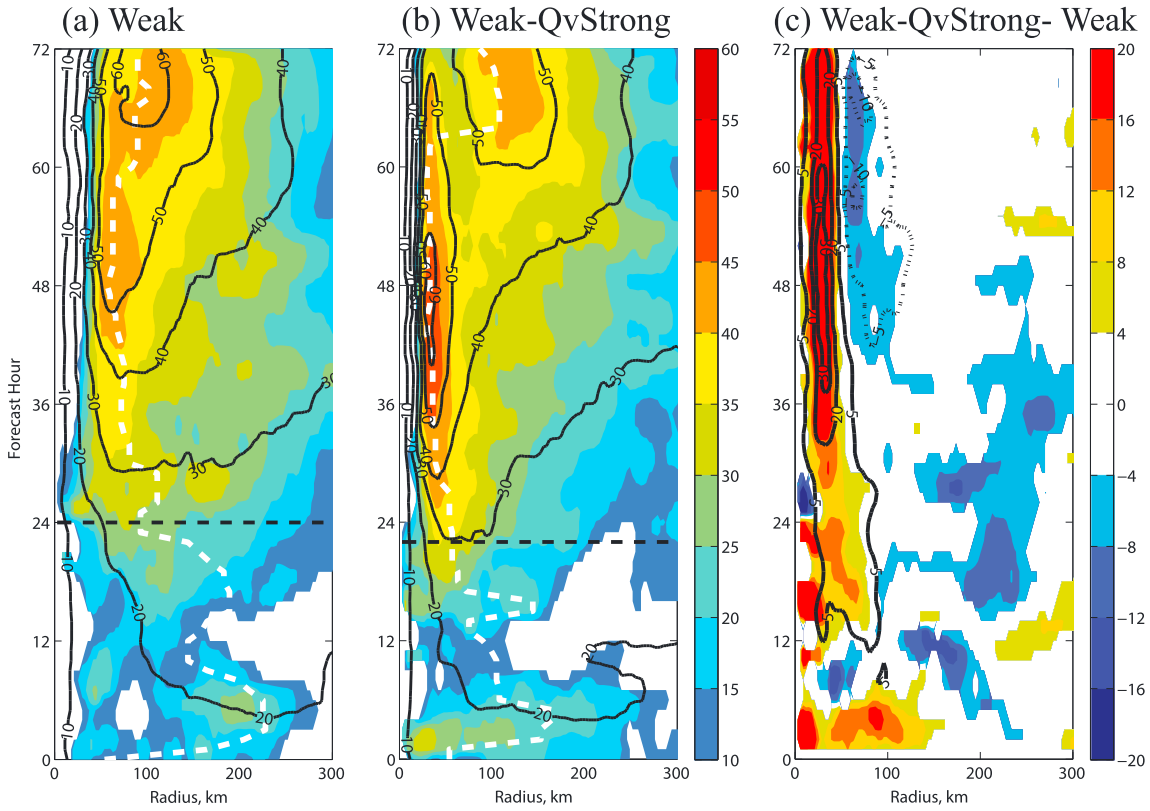

Figure 13. Evolution of the azimuthally averaged composite reflectivity and tangential wind speed (at 1-km height) for (a) Weak, (b) Weak-QvStrong, and (c) differences between the Weak-QvStrong and Weak simulations. The solid (dotted) contours represent positive (negative) values. The white and horizontal black dashed lines indicate the location of radius of maximum wind speed and rapid intensification onset timing for each simulation, respectively.

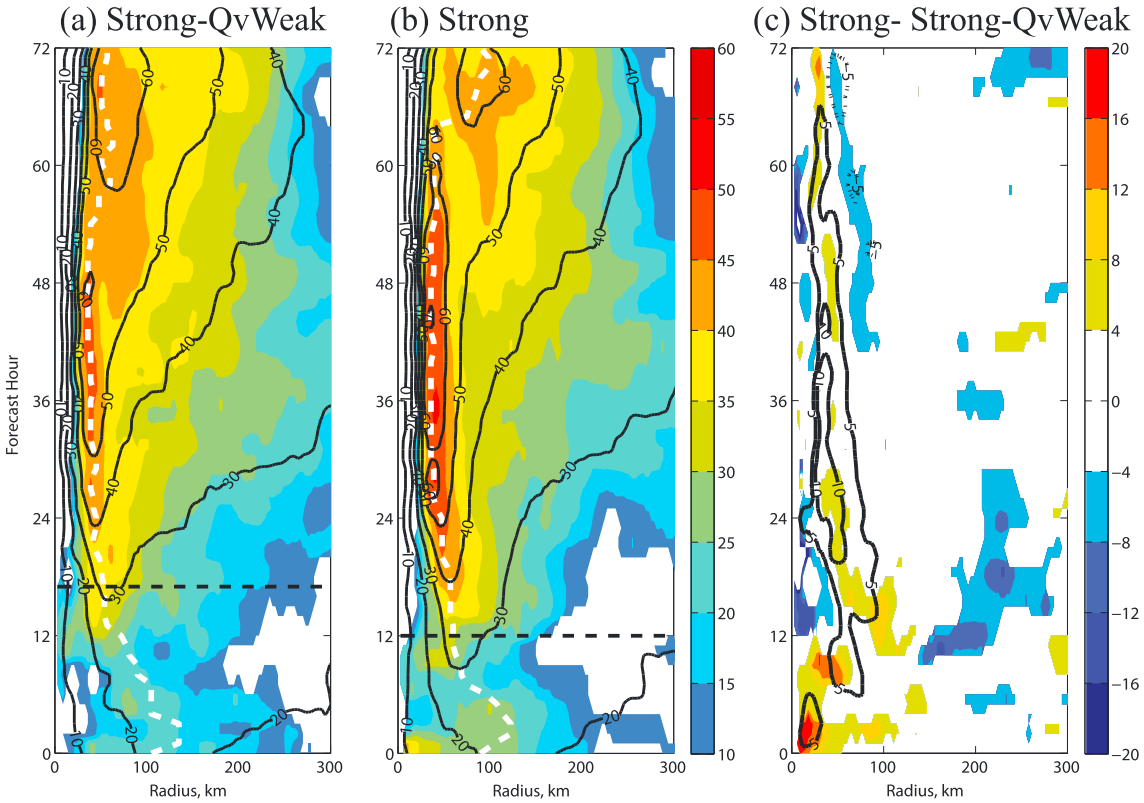

Figure 14. Evolution of the azimuthally averaged composite reflectivity and tangential wind speed (at 1-km height) for the (a) Strong, (b) Strong-QvWeak, and (c) differences between Strong and Strong-QvWeak simulations. The solid (dotted) contours represent positive (negative) values. The white and horizontal black dashed lines indicate the location of radius of maximum wind and rapid intensification onset timing for each simulation, respectively.

The tracks and intensities obtained from the sensitivity simulations are shown in Figure 12. The tracks of the TC from the sensitivity simulations were very close to those from the original simulations. This is reasonable since the track of a TC is mostly dominated by the environmental steering flow, which was outside the inner-core vortex. The Weak-QvStrong began RI 2 hr earlier than the Weak simulation, and the intensities of these two simulations differ by 10 hPa between 6 and 30 hr. The intensity differences were larger at later times (e.g., 20 hPa at 36 hr). Similarly, the Strong-QvWeak predicted that the RI onset 5 hr later than the Strong simulation, and the predicted intensities differed by around 10 hPa for most of the simulation period. The results of our sensitivity analysis demonstrate that a quicker (slower) RI onset and stronger (weaker) TC intensity can be partially attributed to the rich (poor) initial inner-core moisture field.

The impact of the initial moisture on the TC vortex development can be further understood by consulting Figures 13 and 14, which show, respectively, the evolution of the azimuthally averaged tangential wind at 1 km and the azimuthally averaged maximum radar reflectivity of four simulations, and the differences between these fields. The Weak and Strong simulation were initialized with convection scattered across the region defined by, respectively, a 200-km radius (Figure 10a) and a 150-km radius (Figure 10e). With greater moisture in the Weak-QvStrong simulation, more convection within the 100-km radius of the surface center is observed for the first 6-hr simulation, as shown in Figure 13c. We can confidently attribute the increased inner-core convection in the Weak- QvStrong simulation to the variation in the moisture content because the values of the other fields were identical. The tangential wind fields were nearly identical for the first 6 hr of the Weak and Weak-QvStrong simulations, and then the effects of the increased inner-core convection began to propagate, making the tangential wind within the 100-km radius of the Weak-QvStrong simulation stronger than that of the Weak simulation (Figure 13c). The Weak-QvStrong simulation had markedly stronger tangential winds after 24 hr and formed an eyewall earlier than the Weak simulation. In addition, the final radius of the maximum wind of the Weak-QvStrong simulation was around 40 km, which is smaller than that of the Weak simulation (60 km). The smaller eyewall may have been a contributing factor

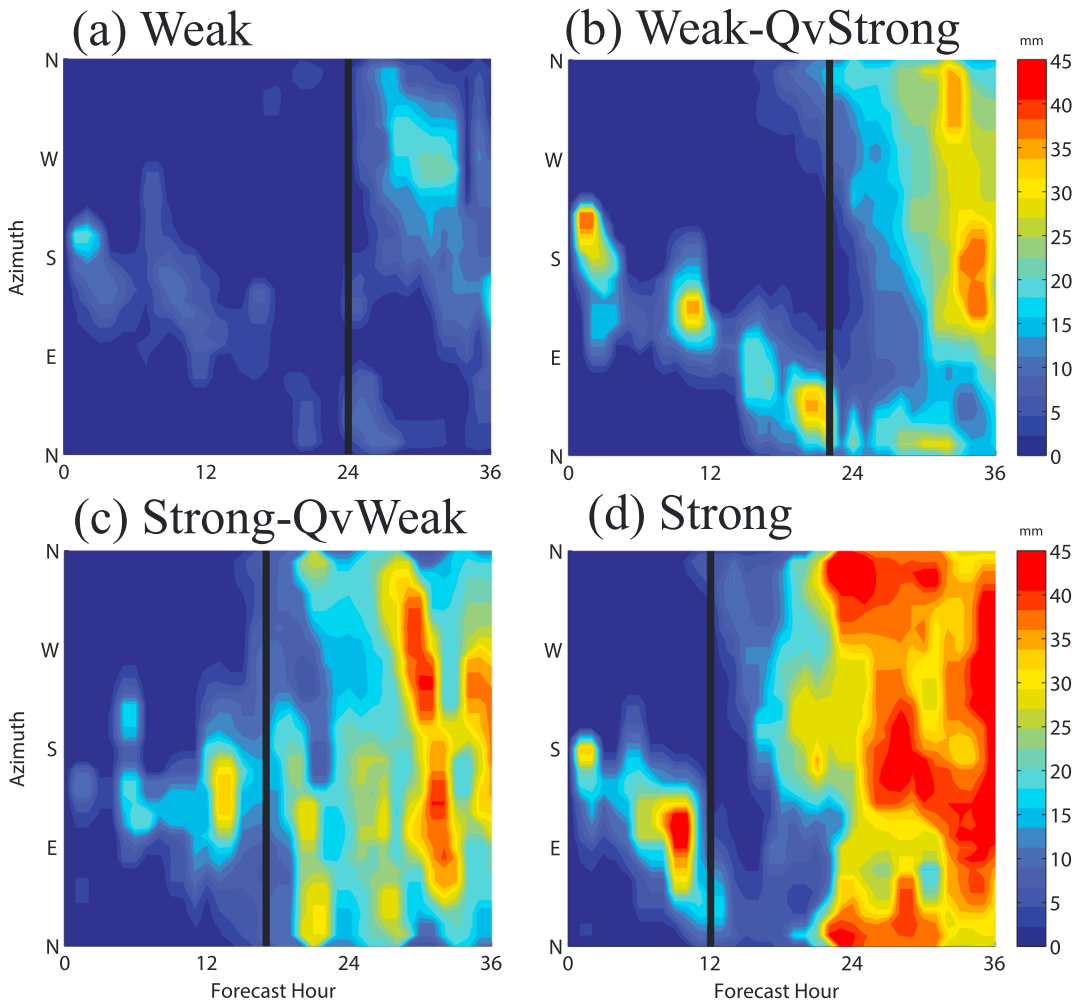

Figure 15. Azimuth-time plot of the precipitation averaged over a 50-km radius for four simulations (a) Weak, (b) Weak-QvStrong, (c) Strong-QvWeak, and (d) Strong. The black vertical line indicates the rapid intensification onset timing in each simulation.

to the large differences between the intensity and intensification rate of the Weak and Weak-QvStrong simulations. Wang and Heng (2016) suggested that convection inside the radius of the maximum wind favors contraction of the eyewall and thus a larger intensification rate due to the larger inertial stability inside the inner core. Shen (2006) also applied the maximum potential intensity theory proposed by Holland (1997) and discovered that a TC with a smaller eyewall can achieve a larger maximum intensity. The Strong and Strong-QvWeak simulations are similar in this regard. After the model initialization, the strength and location of the convection changed quickly in response to the initial moisture distribution (Figure 14c). The tangential wind fields did not vary significantly until a few hours later. The decreased convection in the Strong-QvWeak delays the RI onset by 5 hr and forms the eyewall more slowly than the Strong simulation. Therefore, the initial moisture had an immediate effect on the convection, while the TC vortex (represented by tangential wind fields) took a few hours to respond to the changes in convection (Figures 13c and 14c). The variation in moisture content also affected the final structure of the tangential wind field, which caused the simulations with the Qvapor from the Weak simulation (Weak and Strong-QvWeak) to have a broader eye and a looser tangential wind structure. Conversely, the simulations with the Qvapor from the Strong simulation (Strong and Weak-QvStrong) had a tightened eye and a tightened tangential wind field structure.

We investigated the changes in structure of the convection by plotting the evolution of the precipitation within a 50-km radius along the azimuth in Figure 15. We obtained similar results by reproducing this plot

with a larger averaging radius (e.g., 100 km; not shown). With the Qvapor from the Strong simulation, the convection of the Weak-QvStrong simulation, plotted in Figure 15b, increased immediately and extended further to the east of the surface center, thus underwent axisymmetrization earlier. Though there was only a 2-hr difference between the RI onset timings of the Weak and Weak-QvStrong simulations, the strength and structure of convection within 50-km radius is changed dramatically before and after the RI onset. Similarly, compared to the Strong simulation, the moisture from the Weak simulation had a strong effect on the Strong-QvWeak simulation, considerably weakening the strength of the convection within the 50-km radius and delaying axisymmetrization. Figures 15c and 15d show that the convection in the Strong-QvWeak simulation cannot restore the strength as in the Strong simulation even after the RI onset. Switching the Qvapor in Weak and Strong simulations did not only change the strength and structure of the inner-core convection during the early stages of the simulation but also conveyed the variation to the later stages of the simulation, even after the onset of RI. We hypothesize that the variations between the convection are amplified by a mechanism that provides continuous feedback between the convection, surface wind, and surface enthalpy flux. This mechanism is known as wind-induced surface heat exchange feedback (Emanuel, 1989; Zhang & Emanuel, 2016), but we did not examine it in this study.

It is also worth mentioning that two of the simulations (Weak-QvStrong and Strong) produced secondary eyewall formations, while there was no clear evidence of such formations in the other two simulations (Strong-QvWeak and Weak). Considering the chaotic nature of moisture and limited predictability of secondary eyewall formation in a sheared TC (Zhang et al., 2017), impacts of moisture on secondary eyewall formation are beyond the scope of this study.

6. Concluding Remark

We analyzed the dynamics and predictability of the RI of Super Typhoon Usagi (2013) by conducting data assimilation experiments with the PSU WRF-EnKF TC analysis and forecasting system, a 60-member convection-permitting ensemble, and two sensitivity experiments. The assimilation of the AMVs dramatically improved the forecasts of the RI onset and vortex intensity. We also demonstrated that the predictability of the RI of Usagi was closely associated with the ICs, including the vortex intensity and inner-core moisture content. However, it is important to stress that these two important factors only account for some of the error sources. The uncertainties introduced by the model resolution and physics, as well as observation errors, may also cause the simulated results to differ from the observation data.

Usagi underwent a super RI process as it developed into a category 4 Super typhoon on the Saffir-Simpson hurricane wind scale. The explosive intensification occurred under extremely favorable environmental conditions, with a weak vertical wind shear and a warm ocean surface temperature (>30span>/span>). The numerical forecast of Usagi has its unique challenge of early-predicting the intensification process. In the CNTL simulation, which we obtained from the global ICs, prediction of the RI onset time was 18 hr early, and 40 hPa (minSLP) lower than that of the best track at 0000 UTC 19 September.

Assimilating the Multifunctional Transport Satellite-2 AMV data with the PSU WRF-EnKF system systematically improved the vortex intensity and structure of Usagi. At each cycle, EnKF analysis increments reduce both the primary and secondary circulations of the overly strong TC vortex. Most increments are constrained to remain near or within the inner-core of the TC circulation, extending from the surface to the tropopause. After 24 hr of continuous EnKF cycling, the intensity of the ensemble mean vortex was much closer to that of the best track and considerably weaker (10 hPa higher in minSLP) than that of the CNTL without assimilating AMVs. The intensification process becomes more likely to be initiated later as the intensity of the initial vortex decreases. We can systematically improve the accuracy of the deterministic forecasts by correcting the vortex strength (intensity). All of the intensity values predicted by the deterministic forecasts initialized from the EnKF analyses improved progressively. Compared with the CNTL, the intensity forecast errors in deterministic forecasts have been reduced by up to more than a half.

We used the ensemble forecasts initialized from the EnKF analysis ensemble to explore the dynamics and predictability of the RI of Usagi. Fifteen out of 60 ensemble members matched the best track intensity reasonably well during the RI period. Although all of the ensemble members successfully underwent an RI process, there was a significant spread in the RI onset timings (by as much as 35 hr) and a huge spread in the

intensities (60 hPa at 0000 UTC 19 September). The rest of this study seeks to identify the factors that determine the variation in the RI onset and TC intensity in this ensemble.

An examination of the environmental effects shows that the deep layer shear remained relatively small throughout the entire RI stage. Figures 7a and 7c show that the tilt magnitudes of every member decreased rapidly after the model initialization, being smaller than 40 km at the RI onset, which are consistent with Munsell et al. (2017). However, the shear/tilt magnitudes were not correlated closely with the RI onset at any time (not shown), which indicates that the RI onset timing does not depend on the tilt magnitude in this case. Furthermore, some members did not undergo RI, even when their tilt magnitudes were already small. A small tilt magnitude is necessary, but may not be sufficient, to trigger an RI process.

Our analysis of the correlation between the initial vortex intensity and the RI onset timing demonstrates that a strong initial vortex is more likely to undergo RI early, which is consistent with previous studies (Emanuel & Zhang, 2016; Miyamoto & Takemi, 2015; Munsell et al., 2017). The spread of initial vortex strengths can partially explain the variability of the RI onset time.

The correlation between the initial RH and the RI onset timing shows that the initial inner-core moisture field can also contribute to the variance of the RI onset timing. We selected a Strong and a Weak simulation from the ensemble and used them to further illustrate the impact of the initial inner-core moisture content on the TC intensification. Despite their similar initial vortex intensities and tilt magnitudes, there were considerable differences between the RI onset timings, and the intensities diverged completely at later forecast times. The convection of the Strong simulation was more intense to the north of the surface center before the RI and became axisymmetric earlier than the Weak simulation. There were large differences between both the low and middle level moisture conditions of the Strong and Weak simulations at the initial time, especially to the north of the vortex. Our two sensitivity simulations (Weak-QvStrong and Strong-QvWeak) showed that changing the inner-core moisture content can have an immediate effect on the structure and strength of the inner-core convection, which is crucial to the vortex axisymmetrization under vertical wind shear, and the subsequent RI onset timing. The differences between the structure and strength of the convection gradually built up systematic differences in the TC vortex (represented by tangential wind field). Therefore, the initial inner-core moisture field plays an important role in modulating the wind field at later times by organizing the inner-core convection. In addition to the inner-core moisture, the moisture in the environment outside the core also plays a role by the ventilation effect (Tang & Emanuel, 2010). However, this effect occurs over a long period, so is not examined here.

In this study, we demonstrated the impact of the ICs on the predictability of the RI of Super Typhoon Usagi (2013). We obtained promising results from this case study by constraining the vortex intensity through assimilating AMVs, which is helpful for forecasting RI scenarios. We found that the initial TC intensity was one of the major sources of errors in the prediction of the TC intensity. This result guided our effort toward improving the forecast by correcting the initial intensity. The results of our sensitivity experiments, based on the Weak-QvStrong and Strong-QvWeak simulations, enabled us to explain how the intensity error grows from the inner-core moisture errors, extending the findings in Emanuel and Zhang (2017). As stated in Emanuel and Zhang (2017), the initial intensity error dominates the intensity errors at the first few days, while "growth of intensity error is at least as sensitive to the specification of inner-core moisture as to that of the wind field." Based on these findings, we clearly need to use more accurate representations of the inner-core moisture field to forecast the development of TCs. However, moisture is among the least well-observed variables in TC inner cores. Although we did not improve the representation of the moisture field by assimilating AMVs, the effects of GOES-16/Himawari-8 infrared radiance on constraining thermodynamic fields in TCs were demonstrated in the pioneering work by Zhang et al. (2016). Future studies will explore assimilating satellite infrared radiance observations to constrain the moisture field in TCs.

Acknowledgments
This work is primarily supported by the National Key Research and Development Program of China under grant 2017YFC1501703, the National Fundamental Research 973 Program of China (2015CB452801 and 2013CB430101), the National Natural Science Foundation of China (grants 41322032, 41275031, and 41230421), and the Open Research Program of the State Key Laboratory of Severe Weather. This research is also partially supported by NASA grants NNX16AD84G and NNX12AJ79G and ONR grant N000140910526. The first author conducts the research while as a visiting scholar at the Pennsylvania State University and is supported by the China Scholarship Council. The first author also thanks James Blose for improving the quality of the manuscript. Computing is performed at the Texas Advanced Computing Center. All data presented are stored and can be accessed through the TACC data archive (http://www.tacc.utexas.edu). The English in this document has been checked by at least two professional editors, both native speakers of English. For a certificate, please see http://www.textcheck.com/certificate/EHj5tb.

References

Barker, D. M., Huang, W., Guo, Y.-R., Bourgeois, A., & Xiao, Q. (2004). A three-dimensional variational data assimilation system for MM5: Implementation and initial results. *Monthly Weather Review*, *132*(4), 897–914. https://doi.org/10.1175/1520-0493(2004)132<0897:ATVDAS>2.0.CO;2

Berger, H., Langland, R., Velden, C. S., Reynolds, C. A., & Pauley, P. M. (2011). Impact of enhanced satellite-derived atmospheric motion vector observations on numerical tropical cyclone track forecasts in the western North Pacific during TPARC/TCS-08. *Journal of Applied Meteorology and Climatology*, *50*(11), 2309–2318. https://doi.org/10.1175/JAMC-D-11-019.1

Braun, S. A., Sippel, J. A., & Nolan, D. S. (2012). The impact of dry midlevel air on hurricane intensity in idealized simulations with no mean flow. *Journal of the Atmospheric Sciences*, *69*(1), 236–257. https://doi.org/10.1175/JAS-D-10-05007.1

Chang, C.-C., & Wu, C.-C. (2017). On the processes leading to the rapid intensification of Typhoon Megi (2010). *Journal of the Atmospheric Sciences*, *74*(4), 1169–1200. https://doi.org/10.1175/JAS-D-16-0075.1

Chen, H., & Gopalakrishnan, S. G. (2015). A study on the asymmetric rapid intensification of Hurricane Earl (2010) using the HWRF system. *Journal of the Atmospheric Sciences*, *72*(2), 531–550. https://doi.org/10.1175/JAS-D-14-0097.1

Chen, X., Wang, Y., Fang, J., & Xue, M. (2018). A numerical study on rapid intensification of Typhoon Vicente (2012) in the South China Sea. Part II: Roles of inner-core processes. *Journal of the Atmospheric Sciences*, *75*(1), 235–255. https://doi.org/10.1175/JAS-D-17-0129.1

Chen, X., Wang, Y., Zhao, K., & Wu, D. (2017). A numerical study on rapid intensification of Typhoon Vicente (2012) in the South China Sea. Part I: Verification of simulation, storm-scale evolution, and environmental contribution. *Monthly Weather Review*, *145*(3), 877–898. https://doi.org/10.1175/MWR-D-16-0147.1

DeMaria, M., Sampson, C. R., Knaff, J. A., & Musgrave, K. D. (2014). Is tropical cyclone intensity guidance improving? *Bulletin of the American Meteorological Society*, *95*(3), 387–398. https://doi.org/10.1175/BAMS-D-12-00240.1

Dudhia, J. (1996). A multi-layer soil temperature model for MM5, paper presented at preprints, The Sixth PSU/NCAR mesoscale model users' workshop.

Emanuel, K. (1989). The finite-amplitude nature of tropical cyclogenesis. *Journal of the Atmospheric Sciences*, *46*(22), 3431–3456. https://doi.org/10.1175/1520-0469(1989)046<3431:TFANOT>2.0.CO;2

Emanuel, K., & Zhang, F. (2016). On the predictability and error sources of tropical cyclone intensity forecasts. *Journal of the Atmospheric Sciences*, *73*(9), 3739–3747. https://doi.org/10.1175/JAS-D-16-0100.1

Emanuel, K., & Zhang, F. (2017). The role of inner-core moisture in tropical cyclone predictability and practical forecast skill. *Journal of the Atmospheric Sciences*, *74*(7), 2315–2324. https://doi.org/10.1175/JAS-D-17-0008.1

Harnos, D. S., & Nesbitt, S. W. (2011). Convective structure in rapidly intensifying tropical cyclones as depicted by passive microwave measurements. *Geophysical Research Letters*, *38*, L07805. https://doi.org/10.1029/2011GL047010

Holland, G. J. (1997). The maximum potential intensity of tropical cyclones. *Journal of the Atmospheric Sciences*, *54*(21), 2519–2541. https://doi.org/10.1175/1520-0469(1997)054<2519:TMPIOT>2.0.CO;2

Hong, S.-Y., Dudhia, J., & Chen, S.-H. (2004). A revised approach to ice microphysical processes for the bulk parameterization of clouds and precipitation. *Monthly Weather Review*, *132*(1), 103–120. https://doi.org/10.1175/1520-0493(2004)132<0103:ARATIM>2.0.CO;2

Jiang, H. (2012). The relationship between tropical cyclone intensity change and the strength of inner-core convection. *Monthly Weather Review*, *140*(4), 1164–1176. https://doi.org/10.1175/1520-0469(1997)054<2519:TMPIOT>2.0.CO;2

Kaplan, J., & DeMaria, M. (2003). Large-scale characteristics of rapidly intensifying tropical cyclones in the North Atlantic basin. *Weather and Forecasting*, *18*(6), 1093–1108. https://doi.org/10.1175/1520-0434(2003)018<1093:LCORIT>2.0.CO;2

Kaplan, J., DeMaria, M., & Knaff, J. A. (2010). A revised tropical cyclone rapid intensification index for the Atlantic and eastern North Pacific basins. *Weather and Forecasting*, *25*(1), 220–241. https://doi.org/10.1175/2009WAF2222280.1

Kieper, M. E., & Jiang, H. (2012). Predicting tropical cyclone rapid intensification using the 37 GHz ring pattern identified from passive microwave measurements. *Geophysical Research Letters*, *39*, L13804. https://doi.org/10.1175/1520-0469(1997)054<2519:TMPIOT>2.0.CO;2

Kieu, C., Tallapragada, V., & Hogsett, W. (2014). Vertical structure of tropical cyclones at onset of the rapid intensification in the HWRF model. *Geophysical Research Letters*, *41*, 3298–3306. https://doi.org/10.1002/2014GL059584

Leighton, H., Gopalakrishnan, S., Zhang, J. A., Rogers, R. F., Zhang, Z., & Tallapragada, V. (2018). Azimuthal distribution of deep convection, environmental factors, and tropical cyclone rapid intensification: A perspective from HWRF ensemble forecasts of Hurricane Edouard (2014). *Journal of the Atmospheric Sciences*, *75*(1), 275–295. https://doi.org/10.1175/JAS-D-17-0171.1

Liu, H., & Li, J. (2010). An improvement in forecasting rapid intensification of Typhoon Sinlaku (2008) using clear-sky full spatial resolution advanced IR soundings. *Journal of Applied Meteorology and Climatology*, *49*(4), 821–827. https://doi.org/10.1175/2009JAMC2374.1

Miyamoto, Y., & Nolan, D. S. (2018). Structural changes preceding rapid intensification in tropical cyclones as shown in a large ensemble of idealized simulations. *Journal of the Atmospheric Sciences*, *75*(2), 555–569. https://doi.org/10.1175/JAS-D-17-0177.1

Miyamoto, Y., & Takemi, T. (2013). A transition mechanism for the spontaneous axisymmetric intensification of tropical cyclones. *Journal of the Atmospheric Sciences*, *70*(1), 112–129. https://doi.org/10.1175/JAS-D-11-0285.1

Miyamoto, Y., & Takemi, T. (2015). A triggering mechanism for rapid intensification of tropical cyclones. *Journal of the Atmospheric Sciences*, *72*(7), 2666–2681. https://doi.org/10.1175/JAS-D-14-0193.1

Munsell, E. B., Zhang, F., Sippel, J. A., Braun, S. A., & Weng, Y. (2017). Dynamics and predictability of the intensification of Hurricane Edouard (2014). *Journal of the Atmospheric Sciences*, *74*(2), 573–595. https://doi.org/10.1175/JAS-D-16-0018.1

Munsell, E. B., Zhang, F., & Stern, D. P. (2013). Predictability and dynamics of a nonintensifying tropical storm: Erika (2009). *Journal of the Atmospheric Sciences*, *70*(8), 2505–2524. https://doi.org/10.1175/JAS-D-12-0243.1

NASA (2013). NASA sees super-rapid intensification of Supertyphoon Usagi. Retrieved from https://www.nasa.gov/content/goddard/nasa-sees-super-rapid-intensification-of-supertyphoon-usagi/

Nguyen, L. T., Rogers, R. F., & Reasor, P. D. (2017). Thermodynamic and kinematic influences on precipitation symmetry in sheared tropical cyclones: Bertha and Cristobal (2014). *Monthly Weather Review*, *145*(11), 4423–4446. https://doi.org/10.1175/MWR-D-17-0073.1

Noh, Y., Cheon, W., Hong, S., & Raasch, S. (2003). Improvement of the K-profile model for the planetary boundary layer based on large eddy simulation data. *Boundary-Layer Meteorology*, *107*(2), 401–427. https://doi.org/10.1023/A:1022146015946

Nolan, D. S. (2007). What is the trigger for tropical cyclogenesis? *Australian Meteorological Magazine*, *56*(4), 241–266.

Onderlinde, M. J., & Nolan, D. S. (2014). Environmental helicity and its effects on development and intensification of tropical cyclones. *Journal of the Atmospheric Sciences*, *71*(11), 4308–4320. https://doi.org/10.1175/JAS-D-14-0085.1

Onderlinde, M. J., & Nolan, D. S. (2016). Tropical cyclone-relative environmental helicity and the pathways to intensification in shear. *Journal of the Atmospheric Sciences*, *73*(2), 869–890. https://doi.org/10.1175/JAS-D-15-0261.1

Ooyama, K. (1969). Numerical simulation of the life cycle of tropical cyclones. *Journal of the Atmospheric Sciences*, *26*(1), 3–40. https://doi.org/10.1175/1520-0469(1969)026<0003:NSOTLC>2.0.CO;2

Parrish, D. F., & Derber, J. C. (1992). The National Meteorological Center's spectral statistical-interpolation analysis system. *Monthly Weather Review*, *120*(8), 1747–1763. https://doi.org/10.1175/1520-0493(1992)120<1747:TNMCSS>2.0.CO;2

Pauluis, O., & Held, I. M. (2002). Entropy budget of an atmosphere in radiative-convective equilibrium. Part I: Maximum work and frictional dissipation. *Journal of the Atmospheric Sciences*, *59*(2), 125–139. https://doi.org/10.1175/1520-0469(2002)059<0125:EBOAAI>2.0.CO;2

Rappin, E. D., & Nolan, D. S. (2012). The effect of vertical shear orientation on tropical cyclogenesis. *Quarterly Journal of the Royal Meteorological Society*, *138*(665), 1035–1054. https://doi.org/10.1002/qj.977

Rios-Berrios, R., Torn, R. D., & Davis, C. A. (2016). An ensemble approach to investigate tropical cyclone intensification in sheared environments. Part I: Katia (2011). *Journal of the Atmospheric Sciences*, *73*(1), 71–93. https://doi.org/10.1175/JAS-D-15-0052.1

Rogers, R. F., Reasor, P. D., & Zhang, J. A. (2015). Multiscale structure and evolution of Hurricane Earl (2010) during rapid intensification. *Monthly Weather Review*, *143*(2), 536–562. https://doi.org/10.1175/MWR-D-14-00175.1

Rogers, R. F., Zhang, J. A., Zawislak, J., Jiang, H., Alvey, G. R. III, Zipser, E. J., & Stevenson, S. N. (2016). Observations of the structure and evolution of Hurricane Edouard (2014) during intensity change. Part II: Kinematic structure and the distribution of deep convection. *Monthly Weather Review*, *144*(9), 3355–3376. https://doi.org/10.1175/MWR-D-16-0017.1

Shen, W. (2006). Does the size of hurricane eye matter with its intensity? *Geophysical Research Letters*, *33*, L18813. https://doi.org/10.1029/2006GL027313

Sippel, J. A., & Zhang, F. (2010). Factors affecting the predictability of Hurricane Humberto (2007). *Journal of the Atmospheric Sciences*, *67*(6), 1759–1778. https://doi.org/10.1175/2010JAS3172.1

Stevenson, S. N., Corbosiero, K. L., & Molinari, J. (2014). The convective evolution and rapid intensification of Hurricane Earl (2010). *Monthly Weather Review*, *142*(11), 4364–4380. https://doi.org/10.1175/MWR-D-14-00078.1

Tang, B., & Emanuel, K. (2010). Midlevel ventilation's constraint on tropical cyclone intensity. *Journal of the Atmospheric Sciences*, *67*(6), 1817–1830. https://doi.org/10.1175/2010JAS3318.1

Tao, D., & Zhang, F. (2014). Effect of environmental shear, sea-surface temperature, and ambient moisture on the formation and predictability of tropical cyclones: An ensemble-mean perspective. *Journal of Advances in Modeling Earth Systems*, *6*(2), 384–404. https://doi.org/10.1002/2014MS000314

Tao, D., & Zhang, F. (2015). Effects of vertical wind shear on the predictability of tropical cyclones: Practical versus intrinsic limit. *Journal of Advances in Modeling Earth Systems*, *7*(4), 1534–1553. https://doi.org/10.1002/2015MS000474

Torn, R. D., & Cook, D. (2013). The role of vortex and environment errors in genesis forecasts of Hurricanes Danielle and Karl (2010). *Monthly Weather Review*, *141*(1), 232–251. https://doi.org/10.1175/MWR-D-12-00086.1

Velden, C., Daniels, J., Stettner, D., Santek, D., Key, J., Dunion, J., et al. (2005). Recent innovations in deriving tropospheric winds from meteorological satellites. *Bulletin of the American Meteorological Society*, *86*(2), 205–224. https://doi.org/10.1175/BAMS-86-2-205

Velden, C., Lewis, W. E., Bresky, W., Stettner, D., Daniels, J., & Wanzong, S. (2017). Assimilation of high-resolution satellite-derived atmospheric motion vectors: Impact on HWRF forecasts of tropical cyclone track and intensity. *Monthly Weather Review*, *145*(3), 1107–1125. https://doi.org/10.1175/MWR-D-16-0229.1

Wang, H., & Wang, Y. (2014). A numerical study of Typhoon Megi (2010). Part I: Rapid intensification. *Monthly Weather Review*, *142*(1), 29–48. https://doi.org/10.1175/MWR-D-13-00070.1

Wang, Y., & Heng, J. (2016). Contribution of eye excess energy to the intensification rate of tropical cyclones: A numerical study. *Journal of Advances in Modeling Earth Systems*, *8*(4), 1953–1968. https://doi.org/10.1002/2016MS000709

Weng, Y., & Zhang, F. (2012). Assimilating airborne Doppler radar observations with an ensemble Kalman filter for convection-permitting hurricane initialization and prediction: Katrina (2005). *Monthly Weather Review*, *140*(3), 841–859. https://doi.org/10.1175/2011MWR3602.1

Weng, Y., & Zhang, F. (2016). Advances in convection-permitting tropical cyclone analysis and prediction through EnKF assimilation of reconnaissance aircraft observations. *Journal of the Meteorological Society of Japan*, *94*(4), 345–358. https://doi.org/10.2151/jmsj.2016-018

Wu, T.-C., Liu, H., Majumdar, S. J., Velden, C. S., & Anderson, J. L. (2014). Influence of assimilating satellite-derived atmospheric motion vector observations on numerical analyses and forecasts of tropical cyclone track and intensity. *Monthly Weather Review*, *142*(1), 49–71. https://doi.org/10.1175/MWR-D-13-00023.1

Ying, M., Zhang, W., Yu, H., Lu, X., Feng, J., Fan, Y., et al. (2014). An overview of the China Meteorological Administration tropical cyclone database. *Journal of Atmospheric and Oceanic Technology*, *31*(2), 287–301. https://doi.org/10.1175/JTECH-D-12-00119.1

Zagrodnik, J. P., & Jiang, H. (2014). Rainfall, convection, and latent heating distributions in rapidly intensifying tropical cyclones. *Journal of the Atmospheric Sciences*, *71*(8), 2789–2809. https://doi.org/10.1175/JAS-D-13-0314.1

Zawislak, J., Jiang, H., Alvey, G. R. III, Zipser, E. J., Rogers, R. F., Zhang, J. A., & Stevenson, S. N. (2016). Observations of the structure and evolution of Hurricane Edouard (2014) during intensity change. Part I: Relationship between the thermodynamic structure and precipitation. *Monthly Weather Review*, *144*(9), 3333–3354. https://doi.org/10.1175/MWR-D-16-0018.1

Zhang, C., Wang, Y., & Hamilton, K. (2011). Improved representation of boundary layer clouds over the Southeast Pacific in ARW-WRF using a modified Tiedtke cumulus parameterization scheme. *Monthly Weather Review*, *139*(11), 3489–3513. https://doi.org/10.1175/MWR-D-10-05091.1

Zhang, F., & Emanuel, K. (2016). On the role of surface fluxes and WISHE in tropical cyclone intensification. *Journal of the Atmospheric Sciences*, *73*(5), 2011–2019. https://doi.org/10.1175/JAS-D-16-0011.1

Zhang, F., Minamide, M., & Clothiaux, E. E. (2016). Potential impacts of assimilating all-sky infrared satellite radiances from GOES-R on convection-permitting analysis and prediction of tropical cyclones. *Geophysical Research Letters*, *43*, 2954–2963. https://doi.org/10.1002/2016GL068468

Zhang, F., Snyder, C., & Sun, J. (2004). Tests of an ensemble Kalman filter for convective-scale data assimilation: Impact of initial estimate and observations. *Monthly Weather Review*, *132*, 1238–1253. https://doi.org/10.1175/1520-0493(2004)132<1238:IOIEAO>2.0.CO;2

Zhang, F., & Tao, D. (2013). Effects of vertical wind shear on the predictability of tropical cyclones. *Journal of the Atmospheric Sciences*, *70*(3), 975–983. https://doi.org/10.1175/JAS-D-12-0133.1

Zhang, F., Tao, D., Sun, Y. Q., & Kepert, J. D. (2017). Dynamics and predictability of secondary eyewall formation in sheared tropical cyclones. *Journal of Advances in Modeling Earth Systems*, *9*(1), 89–112. https://doi.org/10.1002/2016MS000729

Zhang, F., Weng, Y., Sippel, J. A., Meng, Z., & Bishop, C. H. (2009). Cloud-resolving hurricane initialization and prediction through assimilation of Doppler radar observations with an ensemble Kalman filter. *Monthly Weather Review*, *137*(7), 2105–2125. https://doi.org/10.1175/2009MWR2645.1

Zhao, K., Lin, Q., Lee, W.-C., Qiang Sun, Y., & Zhang, F. (2016). Doppler radar analysis of triple eyewalls in typhoon Usagi (2013). *Bulletin of the American Meteorological Society*, *97*(1), 25–30. https://doi.org/10.1175/BAMS-D-15-00029.1